

RESEARCH ARTICLE

10.1002/2016JB013545

Special Section:

Slow Slip Phenomena and
Plate Boundary Processes

Key Points:

- The full spectrum of fault slip behavior from slow- to fast-slip events is observed in laboratory fault zones
- We find clear changes in seismic velocity precursory to the stick-slip failure events
- The evolution of shear stress on a fault can be monitored by P -wave velocity changes during seismic cycle

Correspondence to:

E. Tinti,
elisa.tinti@ingv.it

Citation:

Tinti, E., M. M. Scuderi, L. Scognamiglio, G. Di Stefano, C. Marone, and C. Collettini (2016), On the evolution of elastic properties during laboratory stick-slip experiments spanning the transition from slow slip to dynamic rupture, *J. Geophys. Res. Solid Earth*, 121, 8569–8594, doi:10.1002/2016JB013545.

Received 13 SEP 2016

Accepted 5 DEC 2016

Accepted article online 9 DEC 2016

Published online 23 DEC 2016

On the evolution of elastic properties during laboratory stick-slip experiments spanning the transition from slow slip to dynamic rupture

E. Tinti¹ , M. M. Scuderi^{1,2} , L. Scognamiglio¹ , G. Di Stefano¹ , C. Marone³ , and C. Collettini^{1,2} 
¹Istituto Nazionale di Geofisica e Vulcanologia, Rome, Italy, ²Dipartimento di Scienze della Terra, La Sapienza Università di Roma, Rome, Italy, ³Department of Geoscience, Pennsylvania State University, University Park, Pennsylvania, USA

Abstract The physical mechanisms governing slow earthquakes remain unknown, as does the relationship between slow and regular earthquakes. To investigate the mechanism(s) of slow earthquakes and related quasi-dynamic modes of fault slip we performed laboratory experiments on simulated fault gouge in the double direct shear configuration. We reproduced the full spectrum of slip behavior, from slow to fast stick slip, by altering the elastic stiffness of the loading apparatus (k) to match the critical rheologic stiffness of fault gouge (k_c). Our experiments show an evolution from stable sliding, when $k > k_c$, to quasi-dynamic transients when $k \sim k_c$, to dynamic instabilities when $k < k_c$. To evaluate the microphysical processes of fault weakening we monitored variations of elastic properties. We find systematic changes in P wave velocity (V_p) for laboratory seismic cycles. During the coseismic stress drop, seismic velocity drops abruptly, consistent with observations on natural faults. In the preparatory phase preceding failure, we find that accelerated fault creep causes a V_p reduction for the complete spectrum of slip behaviors. Our results suggest that the mechanics of slow and fast ruptures share key features and that they can occur on same faults, depending on frictional properties. In agreement with seismic surveys on tectonic faults our data show that their state of stress can be monitored by V_p changes during the seismic cycle. The observed reduction in V_p during the earthquake preparatory phase suggests that if similar mechanisms are confirmed in nature high-resolution monitoring of fault zone properties may be a promising avenue for reliable detection of earthquake precursors.

1. Introduction

Earthquakes arise as frictional instabilities along tectonic faults, producing seismic ruptures and in some cases catastrophic natural disasters. The hazard associated with seismic failure has been known for some time; however, recent studies show that fault slip can occur not only seismically (or aseismically, via stable creep) but also through quasi-dynamic processes such as slow-slip events [Hirose and Obara, 2005; Schwartz and Rokosky, 2007; Rubinstein et al., 2010; Beroza and Ide, 2011]. The discovery of these phenomena has fundamentally changed our understanding of how slip can occur on tectonic faults [Obara, 2002; Rogers and Dragert, 2003].

Slow earthquakes represent one mode of the spectrum of observed fault slip behaviors and, like regular earthquakes, can accommodate a significant fraction of a fault's slip budget and moment release [e.g., Peng and Gombert, 2010; Obara and Kato, 2016]. Slow slip has been documented in a variety of tectonic settings including the deeper portion of subduction zones [e.g., Shelly et al., 2006], shallow accretionary prisms [e.g., Obara, 2002; Wallace et al., 2016], major plate boundary faults [e.g., Sacks et al., 1978; Shelly, 2009; Veedu and Barbot, 2016], and intraplate tectonic faults [e.g., Crescentini et al., 1999]. It has also been documented in nontectonic environments such as at the base of glaciers [Ekstrom et al., 2003], landslides [e.g., Schulz et al., 2009], and ancient fault structures reactivated by fluid overpressure [e.g., Das and Zoback, 2013; Guglielmi et al., 2015].

Recent works suggest that slow slip may transfer stress to the seismogenic region of faults and trigger catastrophic earthquakes, such as the 2011 M_w 9 Tohoku Oki earthquake [Kato et al., 2012; Ito et al., 2013; Obara and Kato, 2016] or the 2014 M_w 8.1 Iquique earthquake [Ruiz et al., 2014]. In this context slow slip may provide important information for seismic hazard analysis. Thus, understanding the physics of slow earthquakes and detecting possible precursory changes in fault zone properties [Bouchon et al., 2013] are increasingly important aims [Brodsky and Lay, 2014]. The wide range of environments within which slow slip has been reported

and the observation that it often precedes major earthquakes suggest commonalities in the physical processes of fast and slow ruptures. Many fundamental questions remain, including, for instance, can a given fault patch host both slow slip and dynamic rupture [e.g., *Veedu and Barbot*, 2016] and what physical properties dictate rupture speed in each case?

Over the past 50 years or so, laboratory experiments have made a significant contribution to our understanding of earthquake physics [e.g., *Brace and Byerlee*, 1966; *Scholz et al.*, 1972; *Dieterich*, 1979; *Ruina*, 1983; *Dieterich and Kilgore*, 1994; *Marone*, 1998; *Rosakis et al.*, 1999; *Xia et al.*, 2004; *Lykotrafitis et al.*, 2006; *Di Toro et al.*, 2011; *Johnson et al.*, 2013; *McLaskey et al.*, 2015; *Passelègue et al.*, 2016a]. The mechanics of regular, fast earthquakes in particular are based on laboratory studies of stick-slip frictional instability [e.g., *Scholz*, 2002]. More recently, laboratory observations have begun to illuminate the mechanics of slow slip and oscillatory stable sliding [e.g., *Kapoth and Marone*, 2013; *Ikari et al.*, 2013, 2015; *Leeman et al.*, 2016; *Scuderi et al.*, 2016]. Other experiments have documented a strong relation between acoustic transmissivity and fault strength [*Kame et al.*, 2014; *Nagata et al.*, 2008, 2012], or elastic wave velocities and the evolution of rock damage [*Schubnel et al.*, 2006]. High-velocity friction experiments also show changes in permeability, wave transmissivity, or wave velocity after displacements comparable to natural earthquakes [*Tanikawa et al.*, 2010; *Passelègue et al.*, 2016b]. Recently, laboratory observations have also characterized the evolution of P -wave velocity V_p along experimental faults throughout the seismic cycle. *Kapoth and Marone* [2013] showed that V_p velocity changes are controlled by porosity evolution during the seismic cycle. *Knuth et al.* [2013] showed that changes in P -wave speed and wave amplitude could be explained by changes in grain contact stiffness, crack density, and disruption of granular force chains, based on work by *Jia et al.* [1999]. *Scuderi et al.* [2016] expanded our understanding of the acoustic signature of stick-slip failure and showed that precursory changes in seismic velocities occur for the complete spectrum of laboratory slip behaviors from slow slip to fast, dynamic rupture.

These new results [*Scuderi et al.*, 2016] agree with recent studies on natural faults, where seismic velocity variations are observed in connection with regular earthquakes. Seismic wave velocity changes retrieved with ambient noise correlation procedures have been documented during both slow-slip events and moderate-to-large seismogenic ruptures. Seismic velocity reductions during the coseismic phase have been found for the 2014 M_w 6 South Napa earthquake [*Taira et al.*, 2015], the 2003 M 6.5 San Simeon and the 2004 M 6 Parkfield earthquakes [*Brenguier et al.*, 2008], the 2009 M_w 6.1 L'Aquila earthquake [*Zaccarelli et al.*, 2011; *Soldati et al.*, 2015], and the 2008 M_w 7.9 Wenchuan earthquake [*Chen et al.*, 2010; *Stehly et al.*, 2015], among many others earthquakes. *Brenguier et al.* [2008] interpreted the coseismic changes as related to a damage of shallow layers caused by the ground shaking and coseismic stress change followed by postseismic relaxation. *Zaccarelli et al.* [2011] attributed the velocity reduction to increased crack density or reduced compaction of fault gouge and/or migration of fluids. *Taira et al.* [2015] suggested that fracture damage in shallow rocks due to dynamic stress during the South Napa main shock caused the coseismic velocity reduction and that healing process of damaged rocks caused the postseismic velocity recovery. Furthermore, *Rivet et al.* [2011, 2014] reported seismic velocity reduction during the 2006 M 7.5 slow-slip event in the Guerrero region, Mexico. They observed that the maximum change in seismic velocity is related to the peak in strain rate and attributed these changes in nonlinear elastic deformation to rearrangement of cracks and pores. However, these studies do not document changes in velocity, that exceeding the background noise, prior to the main event, even when an improved daily temporal resolution is applied [*Stehly et al.*, 2015]. *Niu et al.* [2008] document such changes. Their work is the only recent seismological study we are aware of that shows clear excursions in the elastic wave speed prior to earthquake failure. They see changes in the travel time of shear waves a few hours before two small earthquakes located at San Andreas Fault Observatory at Depth (SAFOD) site. They suggested that a change in elastic moduli occurs before rupture due to an increase in microcrack density associated with shear and dilatancy.

In this paper we describe laboratory experiments with simultaneous friction and acoustic measurements on simulated fault gouge that reproduce the complete spectrum of slip behavior from fast-and-audible to slow-and-silent stick-slip cycles. We develop a new technique to characterize the evolution of elastic properties during the seismic cycle based on cross correlation of P -wave coda. Finally, we discuss the applicability of our results to natural faults.

2. Mechanics of Frictional Sliding

The mechanics of frictional stick-slip behavior can be described with rate and state friction constitutive equations [Dieterich, 1979; Ruina, 1983; Gu et al., 1984; Marone, 1998, and references therein]. Equation (1) describes the dependence of the shear stress on fault slip velocity and a state variable θ :

$$\tau = \left[\mu_0 + a \ln \left(\frac{V(t)}{V_0} \right) + b \ln \left(\frac{\theta V_0}{D_c} \right) \right] \sigma_n^{\text{eff}} \quad (1)$$

where the evolution of the shear stress (τ) depends on the friction direct effect a , the friction evolution effect b , the characteristic slip distance (D_c), the slip velocity $V(t)$ referenced to a background slip velocity V_0 , and the effective normal stress σ_n^{eff} . The state variable evolves with time and displacement (at least; other variables are likely to be important too) following a perturbation in velocity or stress, and this evolution is described by differential equations (equations (2a) and (2b)). In the literature, two main forms of state evolution have been considered: one described by the Dieterich “slowness law” (equation (2a)) and the other by the Ruina “slip law” (equation (2b)):

$$\left\{ \frac{d\theta}{dt} = 1 - \frac{V(t)\theta}{D_c} \right. \quad (2a)$$

$$\left\{ \frac{d\theta}{dt} = -\frac{\theta V(t)}{D_c} \ln \left(\frac{\theta V(t)}{D_c} \right) \right. \quad (2b)$$

In this context, the characteristic slip distance, D_c , describes the slip required to renew a population of asperity contacts on an extended solid surface [e.g., Dieterich, 1981], or for shear of a granular aggregate such as fault gouge, D_c represents the slip necessary for porosity and shear localization to reach new steady state conditions [e.g., Marone and Kilgore, 1993; Segall and Rice, 1995; Marone et al., 2009]. The parameter D_c differs from the slip weakening friction distance [e.g., Palmer and Rice, 1973], which represents the slip required for traction to drop from an initial to a final value following slip [Bizzarri and Cocco, 2003].

Because rate and state friction laws account for fault re-strengthening after dynamic failure, they can be used to simulate repeated seismic events [Tse and Rice, 1986]. The sign of the quantity $(a - b)$ discriminates between velocity-weakening behavior $(a - b) < 0$, for which friction decreases with increasing slip velocity and velocity-strengthening behavior $(a - b) > 0$, where the opposite occurs producing stable sliding [e.g., Rice and Ruina, 1983; Gu et al., 1984]. Previous works point out that a material can show both velocity-strengthening and velocity-weakening behaviors [e.g., Marone, 1998]. One way in which this can occur is for rate and state frictional parameters (hereinafter, RSF) to evolve with fluid pressure, effective normal stress, or shear strain (among other rheological and frictional factors) [e.g., Boatwright and Cocco, 1996; Scuderi and Collettini, 2016]. Therefore, the fault response to a dynamic stress perturbation can differ depending on the RSF parameters.

Generally, the condition for instability, for a 1-D elastic system, when sliding velocity is still slow (that is, we exclude the secondary effect of inertia), can be written as

$$k < k_c = \frac{(\sigma_n - P_f)(b - a)}{D_c} = \frac{\sigma_n^{\text{eff}}(b - a)}{D_c} \quad (3)$$

where k is the elastic stiffness of the rock surrounding a fault zone; k_c is the critical rheologic stiffness, representing the fault frictional properties; σ_n is the normal stress; and P_f is the pore fluid pressure [e.g., Gu et al., 1984; Scholz, 1998]. Equation (3) represents very simplified elastic and frictional conditions, but it is generally consistent with more sophisticated models of earthquake nucleation and it is applicable to the slow, early stages of slip nucleation [e.g., Liu and Rice, 2007]. In this context, the ratio $K = k/k_c$ describes the boundary between stable, $K > 1$, and unstable, $K < 1$, behaviors [Ruina, 1983; Gu et al., 1984]. To compare the stiffness of experiments conducted at different normal stress, K can also be evaluated as $K = k'/k'_c$, that is the ratio of the effective elastic stiffness $k' = k/\sigma_n$ and the effective critical rheologic stiffness $k'_c = k_c/\sigma_n = (b - a)/D_c$.

Numerical studies [e.g., Gu et al., 1984; Liu and Rice, 2007, among many others] and few laboratory data [Scholz et al., 1972; Baumberger et al., 1999; Leeman et al., 2016; Scuderi et al., 2016] suggest that the transition from stable to unstable behavior involves a region of oscillatory, quasi-dynamic sliding, near $K = 1$.

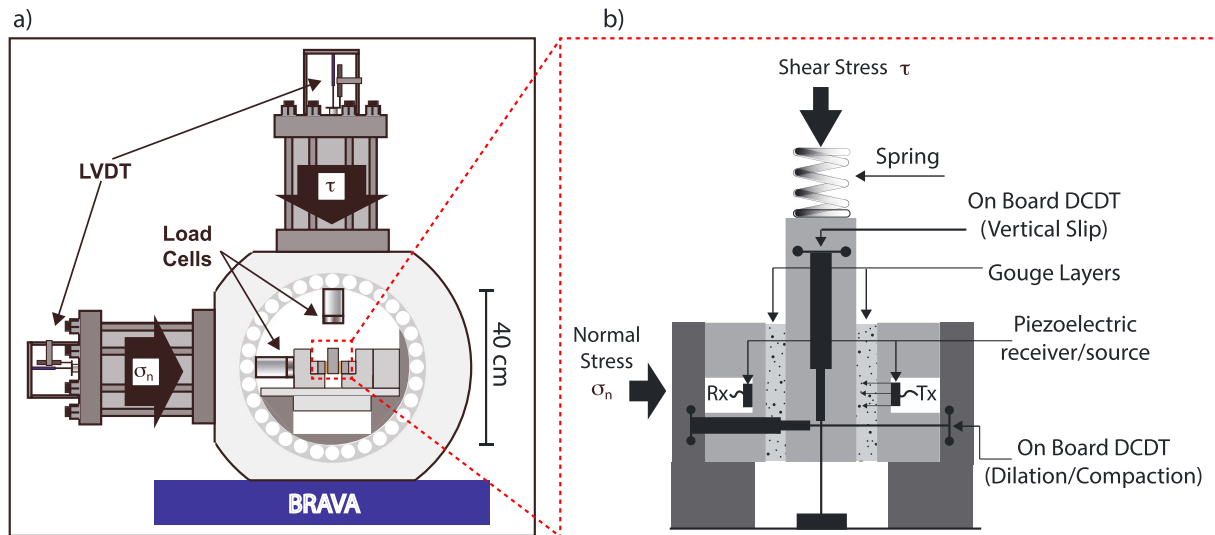


Figure 1. (a) Schematic representation of the biaxial apparatus (BRAVA) configured in the double direct shear configuration. (b) Zoom of the sample assembly showing onboard displacement transducers (direct current displacement transducer) to monitor fault dilation/compaction and true fault slip, PZTs (Tx and Rx) for elastic wave speed measurements, and the compliant spring positioned in series with the central forcing block of the shear assembly, which is designed to de-stiffen the shear loading system.

3. Experimental Methods

We performed laboratory experiments by using a fast-acting, servo-hydraulic biaxial deformation apparatus (Brittle Rock deformAtion Versatile Apparatus (BRAVA); Figure 1a) [Collettini *et al.*, 2014a], on a simulated fault gouge composed of quartz powder in the double direct shear configuration under room temperature and controlled humidity. In order to reproduce both fast and slow stick-slip events we altered the stiffness of the loading machine following the procedures of Leeman *et al.* [2016], with some modifications as described in section 5 below. In addition, we monitored elastic wave speed throughout the experiments, following the approach of Scuderi *et al.* [2016]. In the following we describe the mechanical and ultrasonic data acquisition and analysis.

3.1. Mechanical Experiments

The double direct shear configuration consists of two identical granular gouge layers sandwiched in a three-block assembly, composed of two side stationary blocks and a central forcing block (Figure 1b). In our experiments, gouge layers were composed of powdered granular quartz (Min-U-Sil 40, U.S. Silica Co.), with a mean grain size of $\approx 10 \mu\text{m}$ composed of 99.5% SiO_2 and traces of metal oxides. The forcing blocks are equipped with grooves, 0.8 mm height and 1 mm spacing, perpendicular to the shear direction, to ensure shear localization within the gouge layers and to minimize boundary shear. We constructed gouge layers by using a precise leveling jig to obtain a uniform and reproducible layer thickness of 3 mm and a nominal frictional contact area of $5 \times 5 \text{ cm}^2$. Experiments were run at room temperature and 100% room humidity conditions.

All experiments were performed by using a common procedure. A horizontal servo-controlled hydraulic piston was used to apply and maintain constant load normal to the gouge layers, and a vertical servo-controlled hydraulic piston applied shear load at constant displacement rate. Loads were measured via two strain gauge load cells (accuracy $\pm 0.03 \text{ kN}$) positioned between the ram and the sample assembly. Horizontal and vertical displacements were measured by LVDT (linear variable differential transducers) (Figure 1a), with an accuracy of $\pm 0.1 \mu\text{m}$, referenced at the load frame and the upper side of the ram. Additionally, two short stroke LVDTs were mounted directly on the sample assembly (Figure 1b), avoiding unlikely artifacts from the remote measurement of the LVDT positioned on the external pistons. The first transducer was positioned in the horizontal direction and used to accurately resolve details of sample compaction/dilation. The second transducers was mounted at the top of the shearing block and referenced at the end-platen to measure the true fault slip.

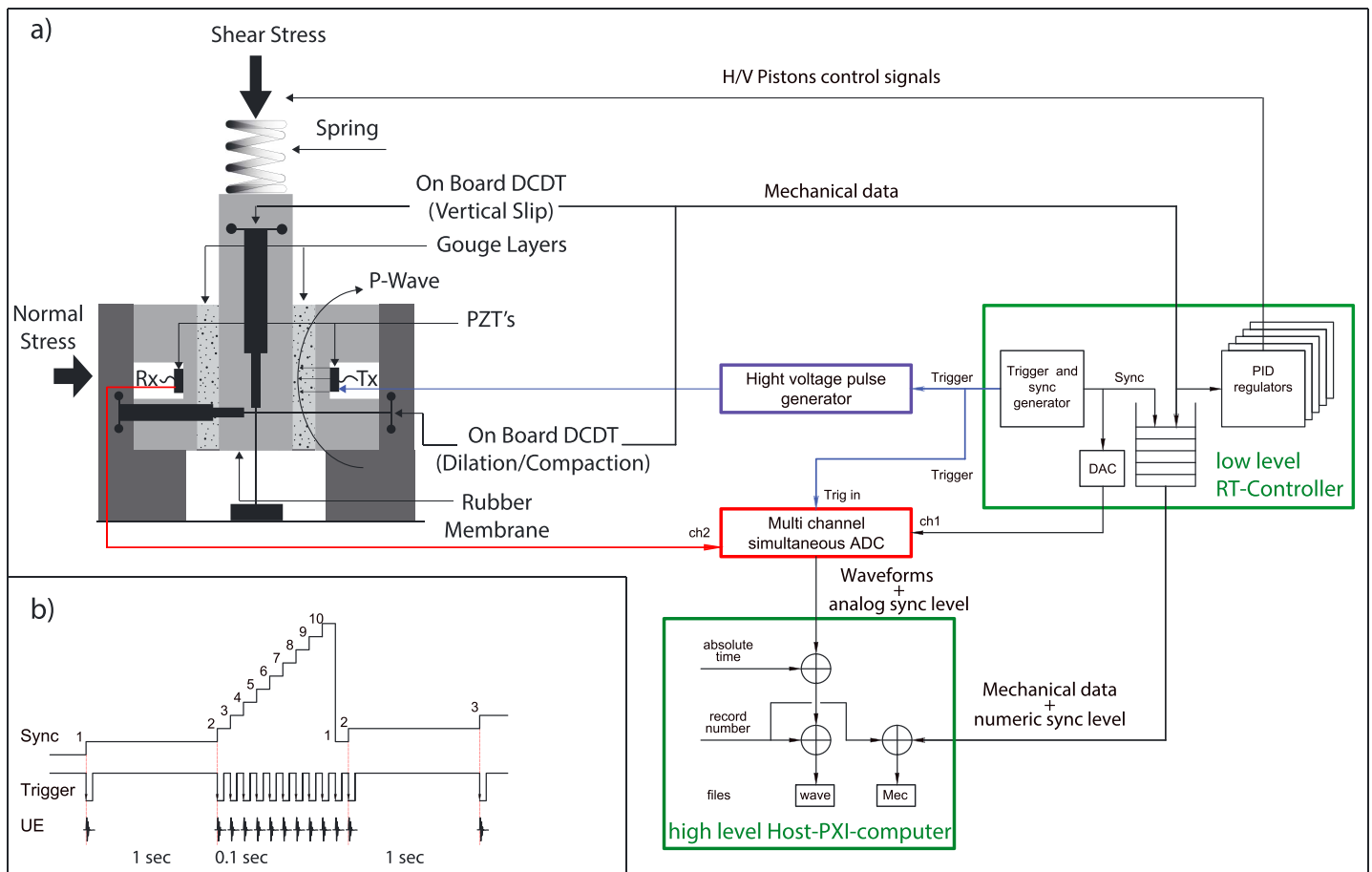


Figure 2. (a) Schematic of the double direct shear configuration with the block diagram showing the main features of the data acquisition system for both mechanical and acoustic data. (b) Sketch of the analog sync, trigger, and ultrasonic emission used to couple mechanical and acoustic data (see text for details).

Our experiments required high-resolution signal measurements and careful synchronization between the mechanical and acoustic data. The block diagram in Figure 2a shows the main features of the data acquisition system (for both mechanical data record and ultrasonic waveform) and the synchronization technique used to match precisely each triggered ultrasonic waveform with the mechanical data record. In the following we describe the main characteristics of both systems and the waveforms synchronization technique used to precisely match mechanical and ultrasonic data (section 3.2).

The mechanical signals (i.e., load cells and LVDTs) were digitalized by a simultaneous multichannel analog to digital (A/D) converter with 24-bit/channel resolution and a sampling rate of 10 kHz. Digital data acquisition was controlled by a low level Real Time (RT) Field Programmable Gate Array (FPGA). Data were collected with a FIFO (First-In, First-Out) buffer and transmitted to the high-level Host-PXI-computer. The raw, 10 kHz, data were then averaged for storage at rates between 1 Hz and 10 kHz. Each data record was marked with a number in succession and stored as a mechanical data file (indicated as Mec in Figure 2).

3.2. Ultrasonic Data Acquisition

During each experiment we generated and recorded ultrasonic waves continuously in order to characterize microphysical processes during deformation. Our sample assembly was equipped with two barium-titanate P-type cylindrical piezoelectric crystals (PI Sensor PIC255, hereinafter PZT) embedded inside cavities on each side-forcing block of the double direct shear assembly, at 13.5 mm distance from the sample (Figure 1b). The transducers are broadband type with thickness of 2 mm and diameter of 20 mm, and resonance frequency of 1 MHz (without constraint). In order to generate P vibrations, the source PZT (Tx) is excited by a very short (≈ 800 ns) high-voltage (300–900 V) electrical pulse provided by a pulse generator (blue box in Figure 2). The pulse generator is triggered by an external signal, coming from a trigger/sync

generator implemented on the FPGA in the RT control system and driven by the sampling clock. The user can change the trigger occurrence during the experiment at frequencies between 0.01 and 100 Hz. Each ultrasonic wave was detected by the receiver PZT (Rx), after passing through the sample assembly and gouge layers, and digitalized by a multichannel 14-bit simultaneous analog to digital converter board (ADLink PXIe-9848) (red box in Figure 2a) with sampling rate settable up to 100 MHz per channel, installed on the Host-PXI-computer.

In our acoustics experiments we used a sampling rate of 50 MHz and an acquisition window of 200 μ s (i.e., 10,000 points per waveform). Because the mechanical and ultrasonic data are acquired with different processes based on different hardware, we were careful to synchronize their acquisition. We employed three levels of synchronization based on three independent numerical markers to stamp the waveform and mechanical records. An absolute time stamp from the Host-PXI-computer clock represents the first level of synchronization. The mechanical record number represents the second level of synchronization and is a sequential number associated with each mechanical record, independent of recording rate. A third level of synchronization consisted of introducing a step sync signal where each level was associated with the mechanical data record and ultrasonic data file. That is, when a trigger signal occurred, we started a one-shot finite acquisition and the sync generator successively increased the sync number by one unit (Figure 2b). The new sync numeric value was added in the FIFO queue, while the analog sync signal level was acquired simultaneously with the Rx ultrasonic signal detected by the receiver PZT. For each trigger a new waveform data record was stored in a binary format file and each data record contained ultrasonic the waveform and numerical markers corresponding to the three levels of synchronization. Thus, for everything we report here, these data represent essentially identical time frames and we can confidently associate variations in acoustic properties with the evolution of mechanical properties.

3.3. Calibration of the Ultrasonic System

We calibrated our loading assembly and ultrasonic system by performing a series of tests to determine the velocity of the forcing blocks and loading assembly. Calibrations included detection of the first arrival of ultrasonic waves that pass through the three steel forcing blocks without gouge layers. We refer to the arrival time of waves as “flight time,” and we define flight time as the time a wave needs to go from the source to the receiver. We conducted calibrations at a series of normal stresses from 5 to 25 MPa, accounting for strain and variations of block thickness. Flight time of the blocks is $t_0 = 13.6 \mu$ s, which corresponds to a V_p for the steel blocks of 5421 m/s, in agreement with expectations for the stainless steel used for the forcing blocks. By accounting for the geometry of the forcing blocks (Figures 1 and 2) we obtain the flight time of each side block as $t_e = 2.464 \mu$ s and of the central block as $t_c = 8.671 \mu$ s.

The calibration procedure was also used to estimate the relationship between P waves and our sample layer thickness. Ideally, the wavelength of the ultrasonic waves should be smaller than the gouge thickness in order to fully capture microphysical variation within the fault zone during shear. The wavelength (λ) depends on the velocity of the material ($V_{p(\text{quartz})}$) and the frequency of the source ($f_{(\text{source})}$) via the relation $\lambda = V_{p(\text{quartz})}/f_{(\text{source})}$. For our experiments the frequency of the source is centered at 1 MHz and the velocity of the quartz gouge layers is ~ 1800 m/s, which yields a wavelength of ~ 1.8 mm. Thus, the wavelength is smaller than the layer thickness for our experiments.

4. Waveform Analysis

4.1. Ultrasonic Data

Once the waveforms were properly synchronized during postprocessing we used them to evaluate variations of elastic properties during each phase of the experiment. Figure 3a shows an example of the evolution of shear traction during an experiment in which several seismic cycles were observed (black line) within a selected time window. The background, colored matrix represents the amplitude map of continuously recorded waveforms, one example of them is shown in gray, with amplitude in volts. This matrix representation allows waveforms from an entire experiment to be visualized and analyzed comprehensively, which is the first step in providing insights on physical processes based on the ultrasonic data.

To investigate the evolution of P -wave velocity during shearing we use cross-correlation techniques. We follow a standard seismic approach wherein a specific pattern of a master waveform (gray line in

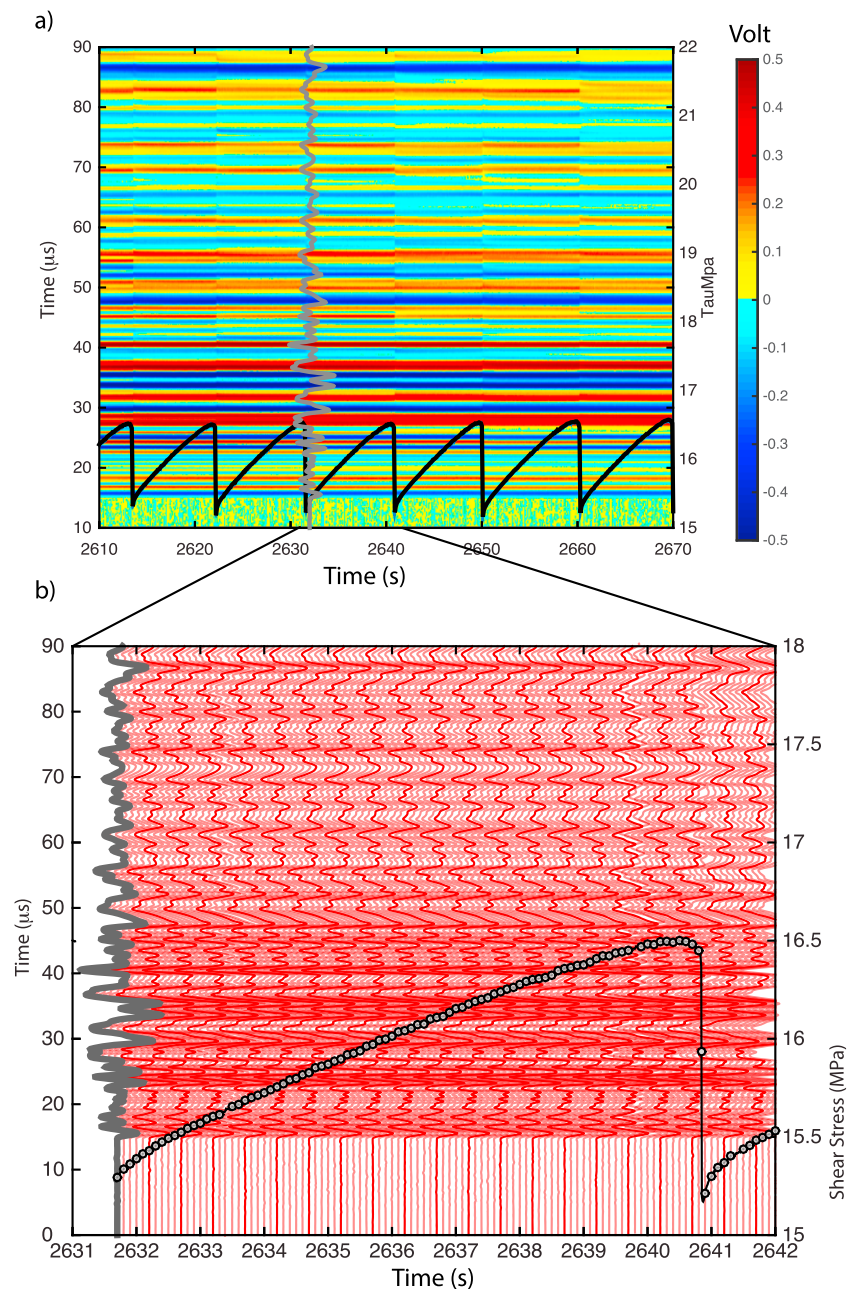


Figure 3. (a) The black curve shows shear stress for stick-slip cycles in a portion of a representative experiment. The background color represents the acoustic wave amplitude as a function of time (left-hand y axis) from continuous records (with scale in volts). A typical waveform is shown in gray. (b) Zoom on a single stick-slip event showing the master waveform in gray at the beginning of the cycle and all the other seismograms in red. The circles on the shear stress curve represent the point at which a waveform was transmitted. For clarity we plotted only one tenth of the waveforms, which were recorded at 100 Hz.

Figure 3b) is compared with successive waves (red lines in Figure 3b) to identify a time-shift. We study *P* waves as well as the *P*-coda arrivals for each of the 20,000+ waveforms recorded in each experiment. For a complete experiment we observe significant evolution of the mechanical and acoustic properties of the fault gouge. Note, for example, the variation in waveform amplitude associated with each stress drop (Figure 3a). To automate the process, we selected a master wave at the beginning of each seismic cycle (Figure 3a). This ensures high cross-correlation values and reduces uncertainties on the estimated flight times.

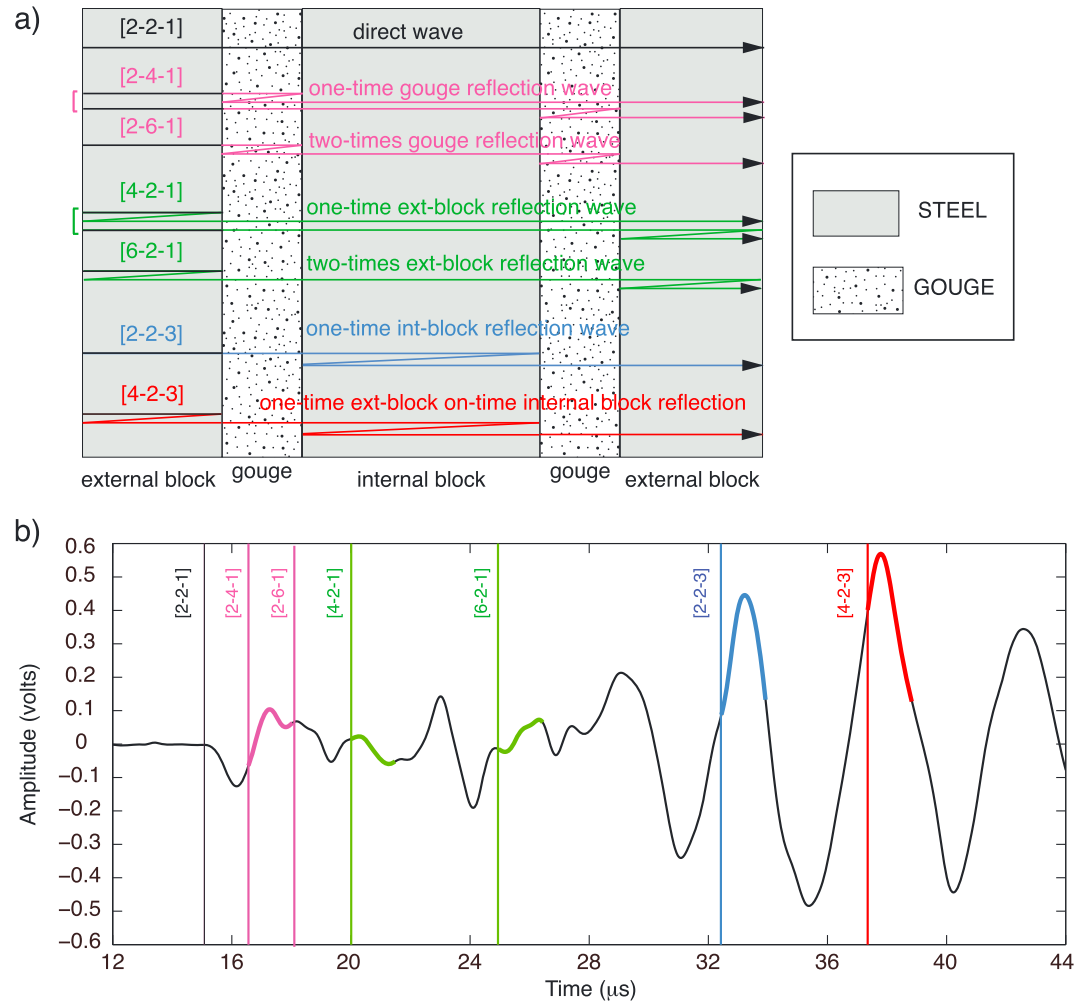


Figure 4. (a) Schematic representation of the double direct shear configuration, showing the propagation model with elastic wave raypaths of the direct wave (black) and several reflected waveforms (colored lines). (b) An example of master waveform indicating the *P*-wave arrival time and the *P*-wave coda theoretical arrivals calculated from equation (5).

4.2. *P*-Wave Properties

We observe systematic changes in *P*-wave properties during shear and throughout the stick-slip cycle (Figure 3). Our approach consists of using a master waveform and cross correlating a time window of $\sim 20 \mu\text{s}$ duration (starting from the *P* arrival) with all the successively recorded seismograms (Figure 3b). This approach produces high-resolution measurements of the variation in-flight time with respect to the master waveform, by determining the time shift needed to yield the highest correlation coefficient. One benefit of cross correlation is that it offers up to a tenfold resolution increase compared to the base data-sampling rate. Thus, we subsampled each seismogram with a 50 \times spline fit prior to cross correlation.

The *P*-wave arrival corresponds to the direct raypath from the Tx to the Rx via the three steel forcing blocks and the two gouge layers. *P*-velocity is obtained by removing the zero time associated with the forcing blocks determined from calibration:

$$V_P(t) = \frac{2h(t)}{T(t) - (t_0)} \quad (4)$$

where $h(t)$ is the instantaneous thickness of one gouge layer, $T(t)$ is the observed *P*-wave flight time, and t_0 is zero time from calibrations (Figure 4).

4.3. Detection of P-Coda Arrival

The results obtained from the cross correlation of the *P*-wave first arrival are usually affected by electrical noise; however, the correlation process returns generally good results with high coefficient. The noise is probably related to electrical and electromagnetic interference between the lines of analog channels (Rx and trigger signals) to the A/D converter (no buffer amplifier is used to drive the 2 m cable for the Rx signal). In addition, the first wavefront arrival contains only limited information of the microphysical changes within the fault gouge because it travels only once through each layer. For these reasons we developed a new approach that allows retrieval of V_p from the *P* coda. We analyze coda waves for any time interval after the first arrival that corresponds to one or more reflections in the sample assembly (Figure 4).

Figure 4a shows a schematic illustration of the sample assembly, denoting the raypaths of transmitted and reflected waves. After the *P*-wave arrival, all the subsequent excitations are due to the summation of destructive and constructive effects of these reflected and transmitted waveforms. We do not expect significant scattering effects from the granular fault gouge because the source frequency, $f = 1$ MHz, is too low in comparison to the grain-size of the gouge. The Tx pulse is radiated normal to the surface of the PZT and therefore perpendicular to the external steel block. Because the rays encounter the fault gouge (which has lower density and lower refraction index than steel) with an incidence angle equal to zero, the transmitted waves maintain the direction and propagate according to Snell's law, with minimum mode conversion.

Our simplified model (Figure 4) assumes that coda waves represent rays that have been reflected and transmitted multiple times within the gouge layers and steel forcing blocks (Figure 4a). In the context of this model equation (5) defines the absolute *P*-wave velocity:

$$V_p(t) = \frac{(N_{g1} + N_{g2})h(t)}{T(t) - [(N_{e1} + N_{e2})t_e + N_c t_c]} \quad (5)$$

where $T(t)$ is the *P*-coda flight time, t_e and t_c are the *P*-wave flight times retrieved from the calibration with no gouge layers; the coefficients N_{g1} , N_{g2} , N_{e1} , N_{e2} , and N_c represent the number of passages along two gouges, two side forcing blocks, and the central block (Figure 4), respectively. The $h(t)$ is the instantaneous layer thickness of one gouge layer, and it is equal to

$$h(t) = H_0 + dh(t) \quad (6)$$

where H_0 is the initial sample thickness that includes systematic and random error, while $dh(t)$ is the thickness variation measured during the experiment.

The main uncertainty in our velocity measurements derives from measurement error of the initial layer thickness. Changes in thickness, $dh(t)$ are tracked precisely throughout each experiment (with accuracy $< 0.1 \mu\text{m}$), while initial thickness is measured by hand with calipers to a precision of ~ 0.01 mm. Uncertainty in the estimation of the flight time is only related with the waveform sample frequency which in our case is 50 MHz resulting in $\pm 2 \cdot 10^{-8}$ s. These uncertainties can influence the absolute accuracy of our wave speed estimates but do not affect the relative changes and short-term trends.

Equation (5) can be used to compute *P*-wave velocity from the first *P* arrival. This corresponds to $N_{e1} = N_{e2} = 1$ (two side forcing blocks), $N_{g1} = N_{g2} = 1$ (two gouge layers), and $N_c = 1$ (one central block) and is represented by the [2-2-1] scheme in Figure 4a. In this case, equation (5) is equivalent to equation (4). As an example, the coda-wave coming from one reflection in the central steel block is [2-2-3]. The arrival times of the raypaths sketched in Figure 4a are shown in the master wave of Figure 4b.

The procedure to retrieve *P*-wave velocity values from variations in *P*-coda arrival times is as follows. We manually select a portion of the experiment to be studied (e.g., inset in Figure 3a). At the beginning of this interval we select a master waveform (Figure 3b). In the master wave we pick the *P*-wave arrival and compute the theoretical arrival times for the early reflections within the gouge (Figure 4a) and plot these arrivals on the master wave (Figure 4b). From the arrivals we select the signal segments with the least noise and the clearest interpretation based on our raypath reflection scheme (Figure 4a). For example, in the master wave of Figure 4b, the segments in blue and red are simpler to cross correlate than those in green because they do not contain wiggles or flex. At this point, we automatically compute (a) the variation in-flight time (*delta flight-time*) required to obtain the best cross-correlation value between the master wave with successive seismograms within the segment of interest (e.g., Figure 3b) and (b) the value of V_p and ΔV_p with respect to the

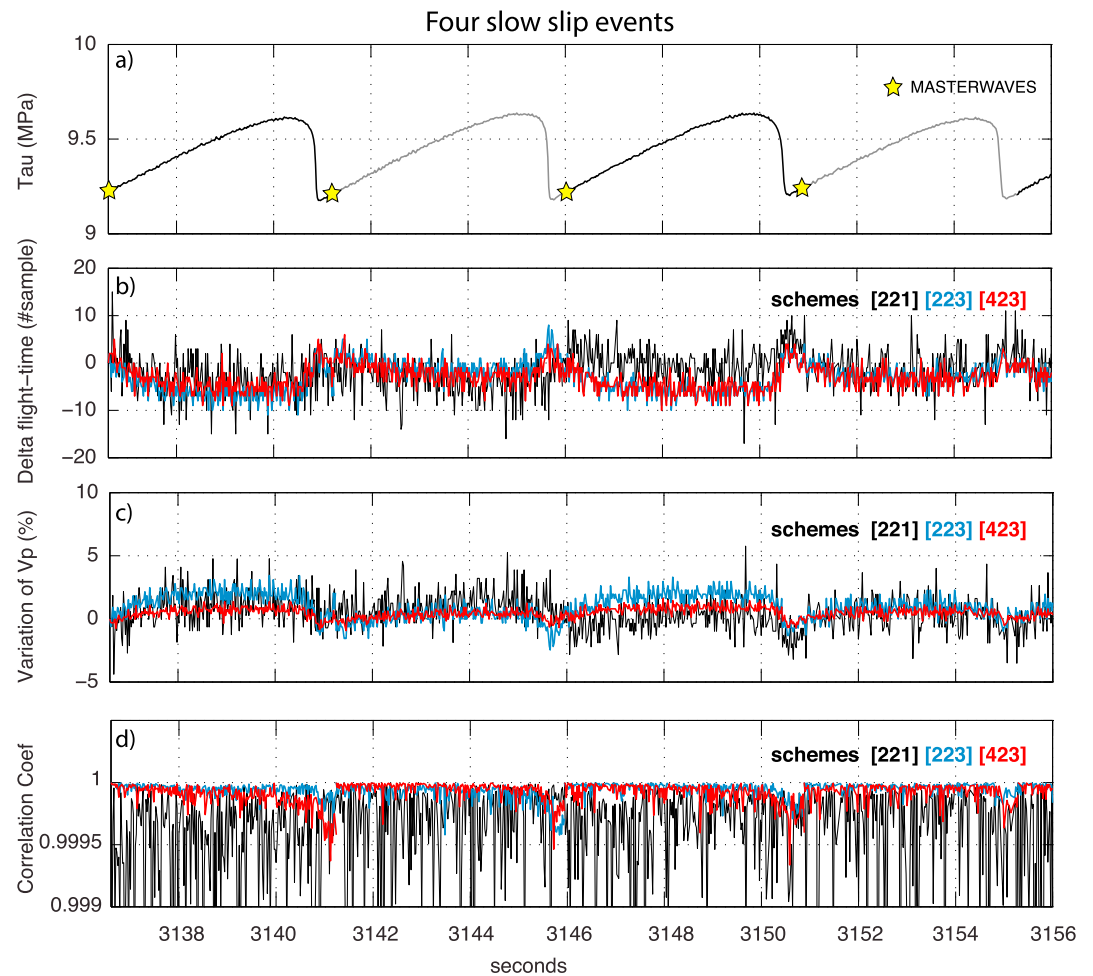


Figure 5. (b) Evolution of delta flight-time, (c) change of P -wave velocity in percentage, and (d) coefficient of cross correlation (d) for (a) four slow-slip events, obtained from the cross-correlation technique by using a wave pattern starting from the P -wave arrival (black) and two P -wave coda (red and blue). The two colored patterns correspond to the reflections schemes indicated in Figure 4a. The yellow stars in Figure 5a represent the position of the master waveforms automatically chosen by the procedure. The sampling period of the recorded waveforms is $2e^{-8}$ s.

master wave, from equation (5). This procedure is repeated for each segment of interest, for example, for each seismic cycle of stick and slip.

An example of the data obtained following the above procedure is reported in Figure 5 where we present cross-correlation results for a few seismic cycles (Figures 5a). The different colors represent different raypath schemes that have been used to compute the *delta-flight time* (Figure 5b), variation of V_p (Figure 5c), and cross-correlation value (Figure 5d). Owing to the similarity of waveforms, maximum correlation coefficients are very high, generally >0.98 . For each scheme, the evolution of both delta-flight time and V_p variation is consistent during the seismic cycles, confirming the reliability of the P -coda procedure. In addition, we highlight that delta-flight time obtained by using P -coda waves, i.e., [223] or [423] schemes, is significantly less noisy than the direct P -wave arrival, i.e., [221] scheme. This is further confirmed by the cross-correlation coefficients of the P -coda waves that are close to 1 and remain constant throughout multiple seismic cycles. Within the V_p coda estimates, subtle differences result from the complexity of the selected waveform segments (Figure 4b); therefore, a careful selection of the waveform is mandatory.

5. Results

We begin by describing the method to determine RSF properties of our simulated fault gouge via velocity step experiments. Then we detail the transition from stable sliding to unstable stick-slip, and creep slip,

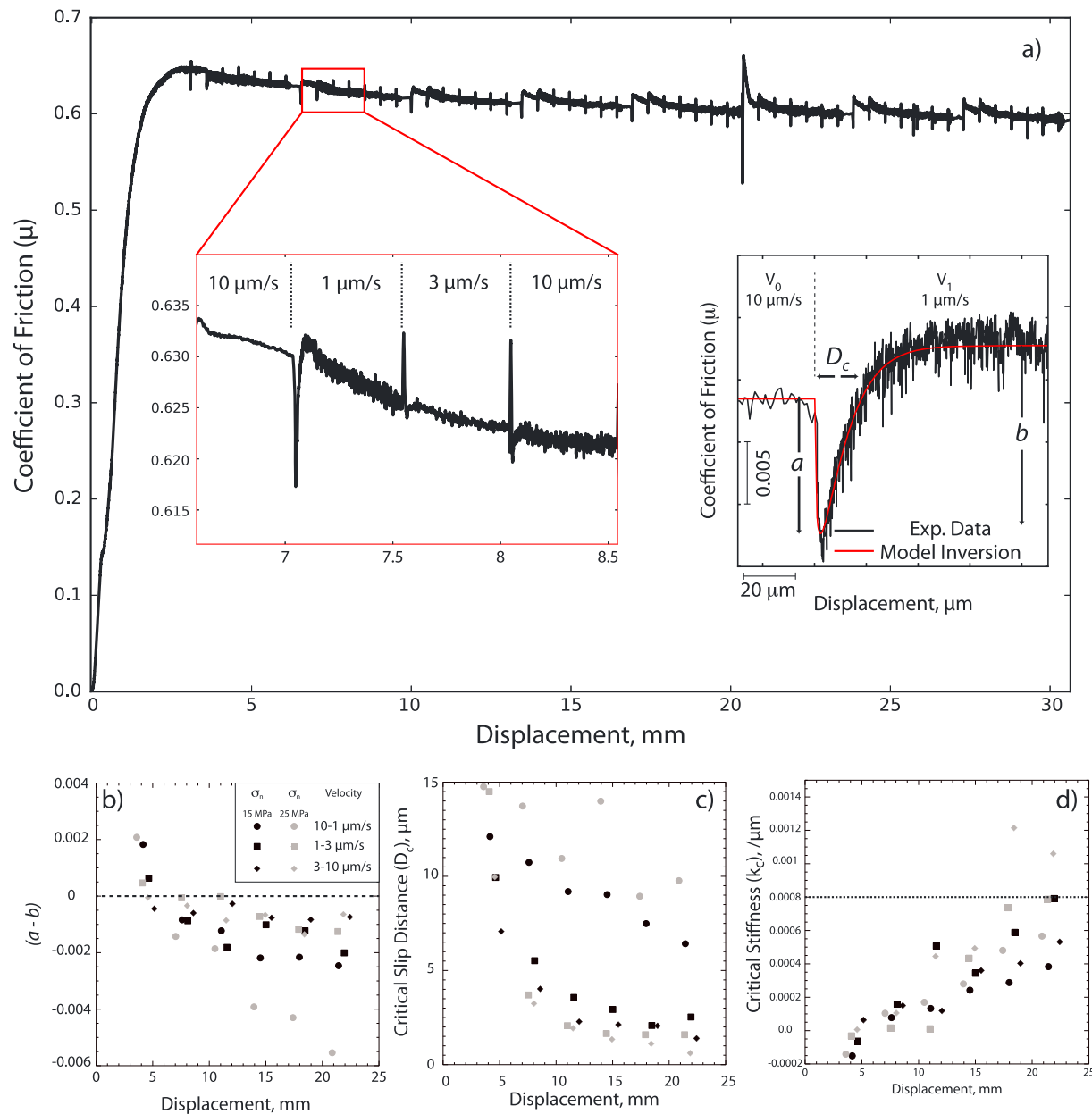


Figure 6. Experimental data and modeling procedure used to obtain the rate and state friction parameters. (a) Typical experimental curve showing the evolution of frictional strength as a function of shear displacement for an experiment performed at $\sigma_n = 25$ MPa (black). The red box highlights representative data for velocity steps from 10 to 1–3–10 $\mu\text{m/s}$. Inset at right shows data and a RSF model inversion (red curve). (b) The friction rate parameter $(a - b)$ shows a transition from velocity strengthening to velocity weakening as shear displacement increases. (c) The critical slip distance (D_c) decreases with increasing displacement. (d) The resulting critical rheologic stiffness, k_c , increases as a function of displacement.

events as a function of shear displacement. The unstable failure events range from dynamic stick slip with audible elastic radiation to silent, slow-slip events, and we show how this transition is related to the ratio of elastic loading stiffness and rheologic stiffness. We study the evolution of kinematic and dynamic failure parameters (e.g., slip velocity and shear stress). Finally, we analyze the evolution of P -wave velocity of the fault gouge during the seismic cycle.

5.1. Mechanical Data

We tested the conditions for frictional stick-slip instability following equation (3). In order to retrieve RSF parameters we performed experiments, at normal stress of 15 and 25 MPa, where the slip velocity was increased

Table 1. Summary of Experiments and Boundary Conditions^a

Experiment Number	Normal Stress (MPa)	Velocity ($\mu\text{m/s}$)	Spring Constant (MPa/ μm)	RH (%)	Comments
i416	15	Run in 10 v.steps 1-3-10	NO	100	Velocity steps
i434	25	Run in 10 v.steps 1-3-10	NO	100	Velocity steps
i266	13	10	0.0296264	100	Stable sliding
i268	13.5	10	0.0296264	100	Stable sliding
i267	14	10	0.0296264	100	Slow slip
i371	15	10	0.0296264	100	Slow Slip
i390	15	10	0.0296264	100	Slow slip
i420	15	10	0.0296264	100	Slow slip
b542	15	10	0.0296264	100	Slow slip
i363	20	10	0.0296264	100	Intermediate
i373	20	10	0.0296264	100	Intermediate
i418	20	10	0.0296264	100	Intermediate
i372	25	10	0.0296264	100	Audible stick slip
i391	25	10	0.0296264	100	Audible stick slip
i415	25	10	0.0296264	100	Audible stick slip
i417	25	10	0.0296264	100	Audible stick slip
i433	25	10	0.0296264	100	Audible stick slip
b519	25	10	0.0296264	100	Audible stick slip
b540	30	10	0.0296264	100	Audible stick slip
b541	35	10	0.0296264	100	Audible stick slip
b543	35	10	0.0296264	100	Audible stick slip
b544	35	10	0.0296264	100	Audible stick slip

^aAll tests were conducted under 100% relative humidity (RH) to ensure experimental reproducibility.

stepwise from 1 to 30 $\mu\text{m/s}$ until we reached a shear displacement of about 30 mm (Figure 6 and Table 1). Each velocity step was then modeled by using a fifth-order Runge-Kutta numerical integration technique with adaptive step size, where the best fit values of the constitutive parameters ($a - b$) and D_c are determined by using an iterative, least squares method (inset in Figure 6a) [Reinen and Weeks, 1993; Blanpied et al., 1998; Saffer and Marone, 2003 for details].

Our data (Figure 6b) show a transition from velocity strengthening, $(a - b) > 0$, to velocity weakening, $(a - b) < 0$, at displacements of about 5–7 mm, and then after a further decrease, the rate parameter tends to be constant at ≈ -0.002 for displacement larger than 15 mm. We document an evolution of D_c from 15 μm to about 1 μm (Figure 6c): most of the reduction occurs in the first 5–7 mm of shear displacement, consistent with previous work [Marone and Kilgore, 1993]. From RSF parameters we calculate the effective critical fault rheologic stiffness, k'_c , as $k'_c = k_c/\sigma_n = (b - a)/D_c$. As the RSF parameters change with displacement, k'_c does the same, and it reaches a threshold value of about $8 \times 10^{-4} \mu\text{m}^{-1}$ after 20–25 mm of shearing (Figure 6d).

To explore the stability transition from stable to unstable frictional sliding we varied the elastic stiffness of the vertical loading column of BRAVA. For the main set of experiments we used a compliant spring ($k = 0.074 \text{ kN}/\mu\text{m}$ or $0.0148 \text{ MPa}/\mu\text{m}$ when cast as the shear stress on one of our $5 \times 5 \text{ cm}^2$ frictional surfaces) in series with the vertical ram to alter the effective stiffness of the loading system k' . We varied the normal stress and took advantage of the evolution with shear of k_c in order to explore a range of conditions around $k/k_c = 1$. Normal stress was held constant at values between 13 and 35 MPa, and shear was induced at constant velocity of 10 $\mu\text{m/s}$ (Figure 7 and Table 1). We observe a spectrum of slip behaviors as a function of $K = k/k_c$, consistent with theory [Gu et al., 1984; Baumberger et al., 1994] and recent experiments [Leeman et al., 2016; Scuderi et al., 2016].

Figure 7 shows typical data for experiments performed at normal stresses ranging from 13 to 35 MPa. Each experiment starts with a loading stage at constant shear velocity until stable sliding shear is achieved, followed by a spontaneous transition to unstable behavior. As normal stress decreases, K increases, and we document a transition from fast, dynamic stick slip, accompanied by audible elastic energy radiation

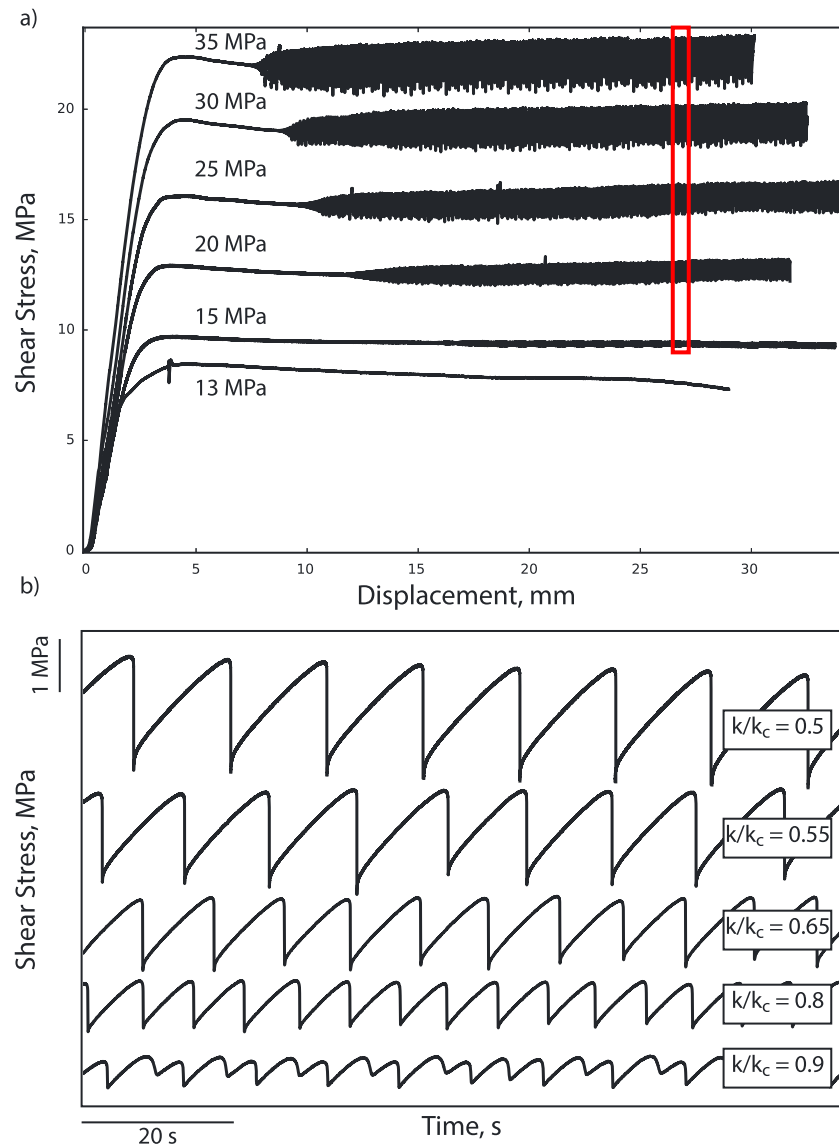


Figure 7. (a) Typical experimental curves showing the evolution of shear stress as a function of displacement for representative experiments at normal stresses, σ_n , that span the transition from fast dynamic stick-slip ($25 < \sigma_n < 35$ MPa) to quasi-dynamic transients at $\sigma_n = 15$ MPa. Sliding is stable at $\sigma_n = 13$ MPa. For each experiment we document a spontaneous transition from stable to unstable behavior with accumulated shear. (b) Zoom corresponding to the red box in Figure 7a. As the stiffness ratio increases (i.e., σ_n decreases) we document a net decrease in stress drop, an increase in stress drop duration and an increase in the frequency of the events. As the stability threshold is approached (i.e., $K \sim 1$) period doubling and amplitude modulation of stress drop arise, reflecting chaotic behavior.

($K < 0.6$), to silent slow-slip events ($0.7 < K < 0.9$). As the stability threshold is approached (i.e., $K \sim 1$) period doubling and amplitude modulation of stress drop arise, reflecting chaotic behavior (Figure 7). When $K > 1$ we observe stable shear. We explored the stability transition in detail and found that it occurred consistently within a very narrow range of normal stresses, between 13.0 and 13.5 MPa, consistent with previous work [Leeman *et al.*, 2016].

Each of our experiments included 200+ slip events (Figure 7), and we measured the effective stiffness k'_{ev} from each loading curve following a slip event. The parameter k'_{ev} represents the combination of the stiffness of the loading system and gouge layers and is measured as the slope of the linear elastic portion of the friction versus shear displacement curves (Figure 8a) using a least squares linear fit procedure. We find that k'_{ev} increases as normal load decreases (Figure 8).

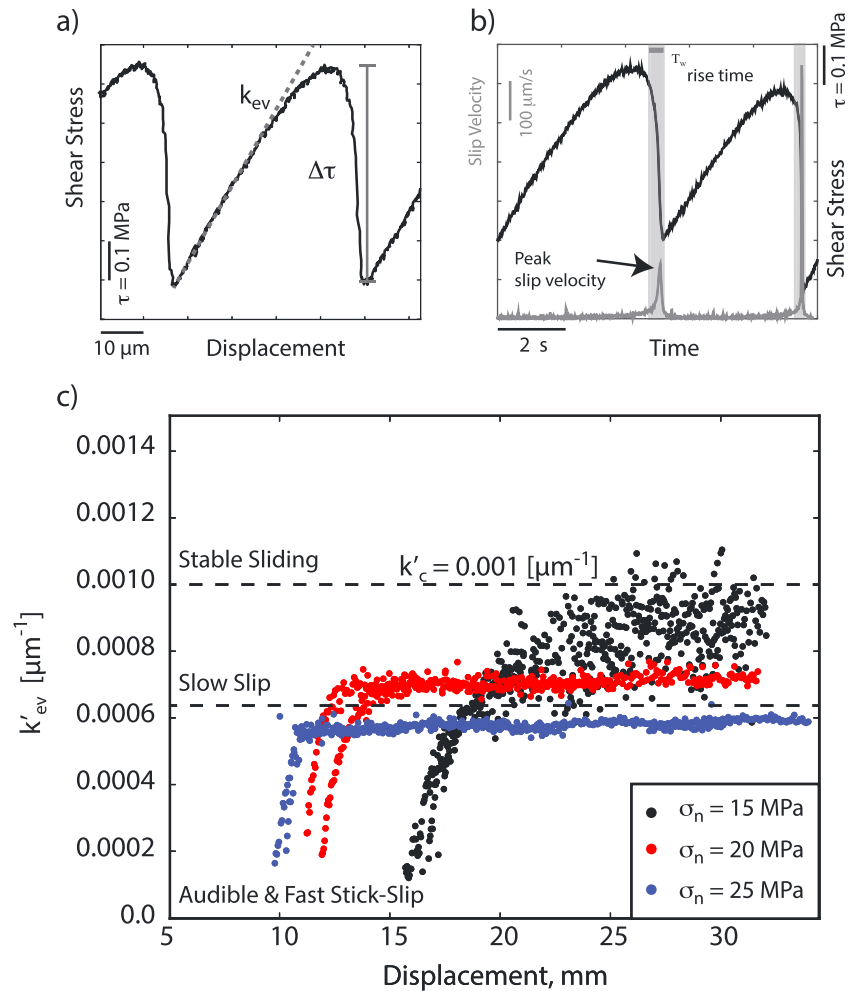


Figure 8. Modeling procedure applied to stick-slip events to retrieve event properties. (a) Evolution of shear stress as a function of displacement for a representative stick-slip event. The dashed gray line represents the linear fit to the linear-elastic portion of the stick-slip cycle, used to obtain the effective stiffness k_{ev} . The vertical gray line shows the stress drop ($\Delta\tau$), measured as the difference between the maximum and minimum shear stress. (b) Evolution of shear stress (black) and slip velocity (gray) during two seismic cycles. The gray vertical stripe defines the event duration or risetime T_w . (c) Evolution of the effective stiffness computed for several slip events during six experiments (Table 1) as a function of shear displacement. We found that the stiffness increases as the normal load decreases up to a threshold value of $\approx 1 \times 10^{-3} \mu m^{-1}$, which allows us to empirically infer the value of k'_c .

Our data show a clear transition between unstable and stable behavior (Figures 7 and 8), which allows us to empirically derive the value of k'_c from the stiffness calculated for each stick-slip event (i.e., top dashed line in Figure 8c). A value of $k'_c \approx 1 \times 10^{-3} \mu m^{-1}$ represents the upper threshold of spontaneous stick-slip events (Figure 8c). This value is quite similar to our measured value of $k'_c \approx 8 \times 10^{-4} \mu m^{-1}$ obtained from velocity step tests using rate and state friction (Figure 6d). Therefore, in this paper we use an averaged k'_c value of $9 \times 10^{-4} \mu m^{-1}$. The stiffness ratio K of each slip event can be computed as the ratio between k'_{ev} measured from stick-slip loading curves and the averaged k'_c .

We measured the systematic changes in stick-slip event properties (Figure 8) as a function of K (Figure 9). Event properties include stress drop $\Delta\tau$, measured as the difference between the maximum and minimum shear stress (Figure 8a), the peak slip velocity, and the event duration or risetime T_w (Figure 8b). We define T_w as the time interval during which the slip velocity is significantly different from zero.

The transition from fast-and-audible to slow-and-silent stick-slip events is well characterized by the evolution of K , T_w , peak of slip velocity as a function of stress drop (Figure 9). As the stiffness ratio K decreases we

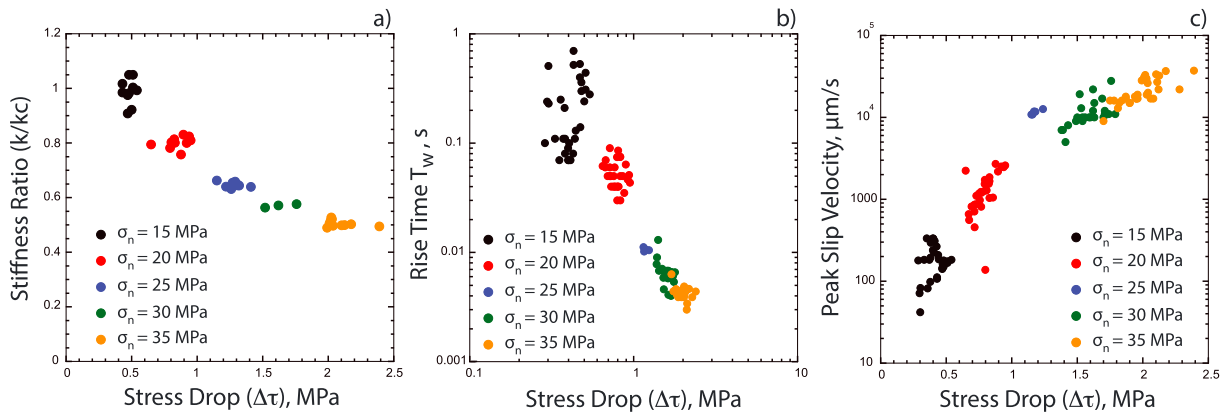


Figure 9. (a) Stiffness ratio, (b) risetime, and (c) peak slip velocity values as a function of stress drop computed for several events from experiments at different normal stress (see Table 1). An increase in stress drop corresponds to a stiffness ratio decrease with a reduction in the risetime and an increase in peak slip velocity.

observe an increase in stress drop from about 0.4 MPa when $K = 0.9$ to ~ 2.0 MPa for $K = 0.5$ (Figure 9a). Events with low stress drop are associated with long durations, up to 0.9 s (Figure 9b), and slow peak slip velocities of 150–200 $\mu\text{m/s}$ (Figure 9c). The largest stress drops occur for the highest normal stresses and lowest values of $K \approx 0.5$ (Figure 9). They are also associated with the highest slip velocities, up to 3 cm/s and shortest slip durations, ≤ 0.003 s (Figure 9).

5.2. Evolution of Elastic Wave Speed During the Seismic Cycle

Here we develop an integrated analysis of the mechanical and acoustic properties (Figure 10). We focus only on experiments at normal stresses of 15, 20, and 25 MPa, corresponding to $K \approx 0.9$, 0.8, and 0.65, respectively, to better characterize the transition from slow-and-silent to fast-and-audible stick slips. From slow- to fast-slip events we observe an increase in the recurrence interval between events, from ~ 3 to 10 s, and in the amplitude of the stress drop, from 0.4 to 1.4 MPa, and slip. Peak slip velocities of slow events are more than 10 times smaller than those for fast events (Figure 9).

The evolution of V_p shows a recurring trend during each seismic cycle resembling the evolution of the mechanical data. P -wave absolute velocity increases from ~ 1.9 km/s at $\sigma_n = 15$ MPa to about 2.6 km/s at $\sigma_n = 25$ MPa, indicating that layer compaction and granular fracturing are greater at higher normal stresses (Figures 10e and 10f). For both slow and fast stick slip there is an initial increase during elastic loading, followed by a decrease prior to failure. Note that V_p reduction in the earthquake preparatory phase is not due to layer dilation since layer thickness is almost constant and abruptly decreases during the stress drop (Figure 10).

To show the details of different slip behaviors from slow to fast, we plot the evolution of mechanical and acoustic data during a single seismic cycle for a range of normal stresses (Figure 11). For each panel of Figure 11, the zero time represents the occurrence of the maximum shear stress and the bottom figures are zooms of the shaded period in the top figures. The blue curves in the bottom figures are slip velocities inferred from displacement recorded with onboard transducers. Each stick-slip cycle (Figure 11) begins with a linear elastic increase of shear stress (black curves), near-zero shear displacement (green curves), and an increase in P -wave velocity (red curves). This is the stick phase of the seismic cycle, when the grains are in a quasi-stationary contact. Slow-slip events are better characterized as creep slip, given that the shear displacement rate between events is nonzero. Our data are consistent with the view that contact junctions grow and stiffen during the interval between failure events. We observe an increase in V_p during this stage. Following the stage of linear-elastic loading, deformation becomes inelastic as the shear stress deviates from linearity and V_p reaches a maximum value. The dotted gray lines in Figure 11 mark the maxima in V_p . For fast-slip events (Figure 11a) V_p remains almost constant at the maximum value until the fault begins to slip and stress reaches a maximum. Then, shear strength and V_p decrease slowly before the abrupt acceleration and stress drop that corresponds with event failure and the main drop in V_p (Figure 11a). For intermediate- and slow-slip events (Figures 11b and 11c) we observe a progressively longer stage where V_p is roughly

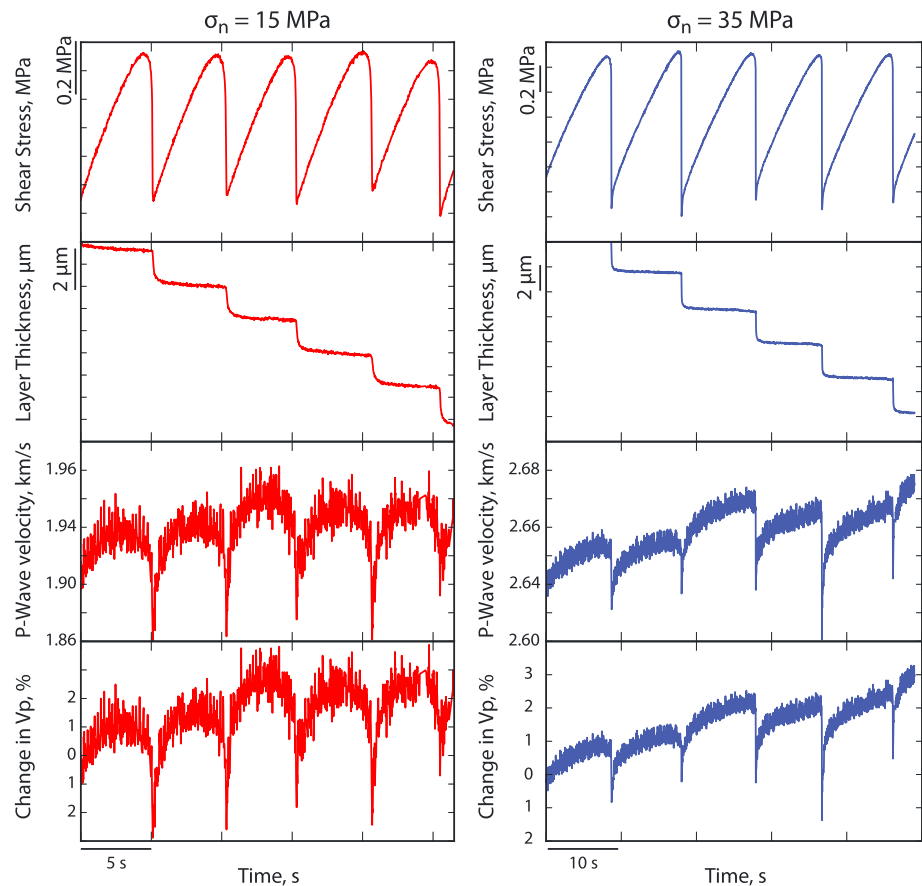


Figure 10. Data showing the evolution of shear stress, layer thickness, slip velocity, and elastic wave speed V_p and ΔV_p (%) during slow (red curves) and fast (blue curves) stick-slip events corresponding to experiments at 15 and 25 MPa. Note that the decrease in V_p during the coseismic phase is always associated with fault gouge compaction.

constant, at the maximum value, and a more pronounced reduction in V_p prior to failure (Figures 11b and 11c). We interpret this stage of the seismic cycle as the creep phase, marked by the onset of nonlinear elastic deformation. Note that the changes in V_p during creep are not associated with macroscopic changes in layer thickness (i.e., no dilation or compaction). During creep acceleration prior to rapid failure, the reduction of P -wave velocity indicates that particle contact junctions are no longer under quasi-stationary contact. Our observations suggest contact yield and rejuvenation of contact junctions, presumably in association with grain boundary sliding, particle rolling, and/or microcracking.

In the coseismic stage, i.e., from maximum to minimum in the shear stress (gray shaded area in Figures 11a–11c, top, zoomed in bottom), the shear stress initially decreases slightly and then it drops abruptly. In the initial stage, which corresponds to the earthquake preparatory phase (i.e., nucleation), accelerated creep coincides with a reduction in P -wave velocity of $\sim 1\%$, (red shaded area in Figures 11a–11c, bottom). Finally, during the shear stress drop we observe strong reduction, 2–3%, in V_p . This is the slip phase, usually called weakening phase, when the fault accelerates from creep to high slip velocity. In this phase the grain contacts within the fault zone are fully renewed. For all the seismic cycles we observe that peak slip velocity (blue curves) is attained before reaching the minimum shear stress. In agreement with mechanical models [e.g., Fukuyama *et al.*, 2003; Tinti *et al.*, 2004], this demonstrates that RSF parameters and the effective normal stress control the slip accelerations as well as the timing of peak slip velocity during the traction drop. In particular, moving from slow to fast events we observe that the occurrence of the peak slip velocity approaches the end of the weakening phase, confirming the results obtained in dynamic theoretical studies [Tinti *et al.*, 2004].

Figure 12 shows data for a set of 30 seismic cycles where red, gray, and blue represent slow-, intermediate-, and fast-slip events, respectively. Each curve is zeroed at the peak stress (green dots), and data are

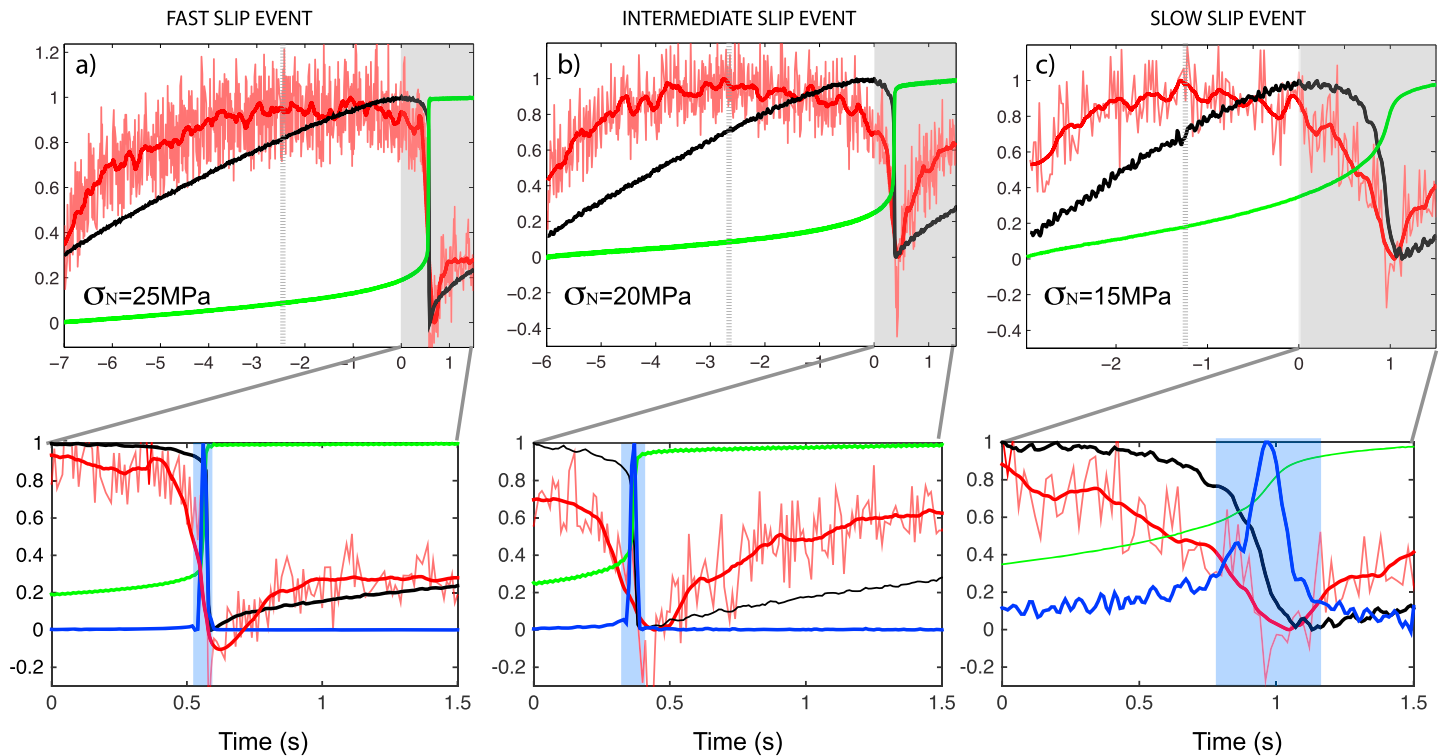


Figure 11. (a–c, top) Evolution of mechanical and acoustic data for a single seismic cycle for three representative experiments at 25, 20, and 15 MPa. Shear stress (black lines), shear displacement (green lines), and V_p variations (red lines) are normalized and superimposed. Zero time represents the occurrence of the maximum shear stress. The gray dotted lines highlight the time where V_p reaches the maximum value. (a–c, bottom) Zoom corresponding to gray boxes in the top figures showing the details of the coseismic phase. The blue lines represent the slip velocity, while the blue boxes identify the different risetime values.

superimposed to facilitate comparison between different values of K and loading conditions. The loading phases of the shear stress curves in Figure 12a display equal slope, confirming similar loading conditions for the experimental faults. The duration of this phase increases with increasing normal stress. Once the peak of stress is reached, weakening begins.

Moving from slow to fast stick-slip events, we observe an increase in slope corresponding to a growth in amplitude of stress drop (Figure 12a). The V_p variation (Figure 11b) mimics the traction evolution, and starting at least from the plotted red line, it shows the already mentioned preparatory phase consisting in a smooth decrease of P -wave velocity before the weakening phase. This is a clear, robust observation across all of the experiments we performed, and we consider this feature as an event's precursor. Consistent with previous results [Scuderi *et al.*, 2016], we find clear precursors to failure for both slow-, creep-slip failure events and fast, stick-slip failure events.

The systematic relationship between shear stress and P -wave velocity during the seismic cycle (Figure 12) for both slow and fast earthquakes suggests a common process for the spectrum of fault slip behavior [e.g., Leeman *et al.*, 2016; Scuderi *et al.*, 2016]. The slip evolution (Figure 11c) is characterized by inelastic slip (creep) before the coseismic phase for all the analyzed seismic cycles, while an evident initial stick phase exists only for fast events. The creep-rate differs between the experiments. Considering that the slipped area and the rigidity of the samples are constant for all the experiments, the differences obtained in coseismic total slip result in different magnitudes for the laboratory earthquakes. Figures 12d–12f show the slip velocities resulting from the stress evolution of our experiments. With increasing normal stress, we move from a smooth slip velocity (similar to a *Gaussian function*), characterized by a long risetime and low peak values, to a sharp slip velocity (similar to a *delta function*) having a short risetime, and high peak values that produce audible slip events. It is noteworthy that the fastest-slip events shown in Figure 9 have peak slip velocity values 10 times larger than those shown in Figure 12f and 100 times larger than those in Figure 12d. The slip rate function associated with dynamic rupture propagation during a real earthquake is poorly known, and it is normally assumed a priori in dynamic models. This assumption induces a limitation in understanding

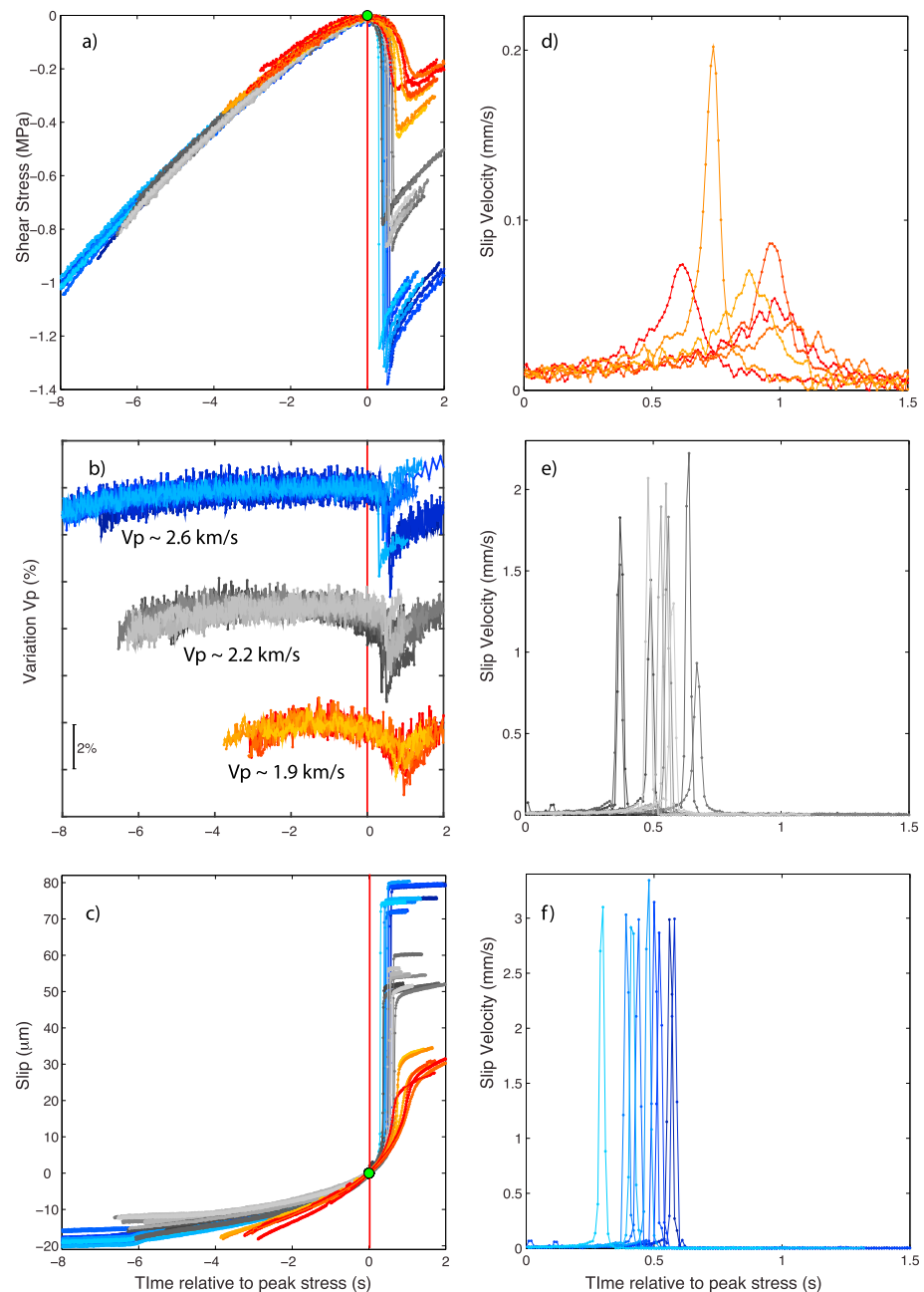


Figure 12. Time evolution of (a) shear stress, (b) V_p variations, and (c) slip for a set of 30 selected seismic cycles for slow (red), intermediate (gray), and fast (blue) events. Each curve is zeroed at the peak stress (green dots). (d–f) The correspondent slip velocities to the stick-slip events shown in Figure 12a.

dynamic fault weakening, and it influences the variability and reliability of estimated source parameters [Tinti *et al.*, 2009]. The characterization of the slip rate function obtained in our experiments (e.g., Figures 12d–12f) can provide significant insights for dynamic earthquake modeling.

6. Discussion

6.1. The Spectrum of Fault Slip Behaviors From Slow to Fast Stick-Slip Events

We have characterized the evolution of mechanical and elastic properties during stick-slip events that span a wide spectrum of slip rates. We systematically varied the slip rate during dynamic and quasi-dynamic failure

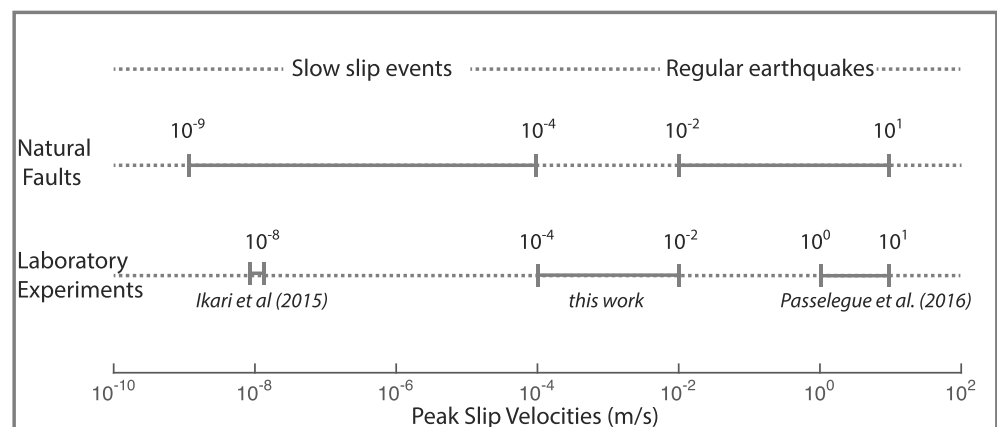


Figure 13. Schematic representations comparing peak slip velocities of slow-slip events and regular earthquakes for natural faults and laboratory experiments. The peak slip velocities recovered in this study are consistent with the values marking the transition found in nature between slow and regular earthquakes.

by altering the stiffness of our loading system to explore the transition from slow-and-silent to fast-and-audible stick-slip events. In our experimental range (Figure 7) the fastest stick slips show recurrence interval of about 15 s and stress drop in the order of 2 MPa. These failure events have risetimes of ≈ 0.003 s with peak slip velocity of up to 3×10^{-2} m/s (Figure 9). The slowest slip events are characterized by recurrence intervals of ≈ 5 s and stress drops of ≈ 0.5 MPa. The risetime for slow events is ≤ 0.9 s, and peak slip velocity for these events reaches 10^{-4} m/s.

6.2. Application to Tectonic Faulting

The laboratory slip events are of course interesting in many ways, as they have much to add to our understanding of earthquake physics based on stick-slip friction [e.g., Brace and Byerlee, 1966; Scholz, 2002]. However, the question remains as to whether these experiments, and in particular those showing slow slip, include any of the key processes that produce slow earthquakes in nature and/or are accurate analogs of same. Figure 13 presents a comparison between peak slip velocities reported for laboratory experiments with observations of tectonic fault slip. Our laboratory slip velocities range from 10^{-4} to 10^{-2} m/s (Figure 13) and are consistent with slow-slip velocities [Peng and Gombert, 2010] and the lower end of the slip velocities inferred for regular, fast earthquakes [e.g., Mai and Thingbaijam, 2014].

Our laboratory experiments show slip rates during slow events that are just a few $\mu\text{m/s}$ higher than the background driving rate. Related work by Ikari et al. [2015] has documented slow-slip velocities as low as 10^{-8} m/s using loading rate of 85 mm/yr. It has long been known that laboratory stick-slip events can also reproduce the slip velocities of regular, fast earthquakes, [e.g., Brace and Byerlee, 1966; Scholz et al., 1972; McLaskey et al., 2015; Passelegue et al., 2016a]. Thus, at the most basic level, our observations are consistent with the range of slip rates observed for the spectrum of fault slip behaviors (Figure 13). While it is clear that laboratory studies have provided fundamental insights for the mechanics of fast earthquakes, the question remains as to whether the same is true for slow earthquakes and the full spectrum of fault slip rates. Again, the data of Figure 13 indicate only that the range of slip rates observed near the stability transition, i.e., $K = 1$, is consistent with the range of fault slip behaviors observed in nature.

Our laboratory data indicate that fault slip behavior is controlled by the interaction between fault frictional rheology and local elastic properties of the fault zone and wall rock, in agreement with theoretical predictions [Gu et al., 1984], numerical studies [Liu and Rice, 2007; Rubin, 2008; Segall et al., 2010], and previous experiments [Scholz et al., 1972; Leeman et al., 2016; Scuderi et al., 2016]. In particular, we document in detail the stability transition near $K = 1$ and find multimode fault slip behavior (Figure 7) as it has been observed in different fault rock material, including granites [Scholz et al., 1972] and serpentinites [Kaproth and Marone, 2013]. These observations show that the stiffness ratio K is the key parameter in the laboratory. As applied to natural faults, our data would suggest that K could provide a general mechanism for the observed spectrum of tectonic fault slip behaviors. This mechanism, associated with the range of behaviors observed

around the frictional stability transition, could act in concert with dilatancy hardening and other mechanisms that have been proposed for slow slip based on slip rate dependence of the friction rate parameter ($a - b$) and k_c [e.g., Liu and Rice, 2007; Segall et al., 2010; Knaproth and Marone, 2013]. In this context the major factors dictating the mode of fault slip are frictional properties, effective normal stress, and elastic stiffness of the fault zone. Previous works have suggested that elevated fluid pressure occurs in slow-slip regions, which would decrease the effective normal stress [Shelly et al., 2006; Zoback et al., 2012; Guglielmi et al., 2015]. Fault zone width and maturity may also play a role because they affect friction constitutive parameters [e.g., Marone et al., 2009] and elastic stiffness [Bilek and Lay, 1999], as documented in our experiments (Figure 6). Our results suggest that the stability parameter K includes all of these characteristics as applied to tectonic faults.

Taken together with the standard theory of earthquake physics based on frictional stick slip, our work suggests that interaction between fault zone stiffness and fault rheology can dictate the mode of fault slip, ranging from slow-slip and quasi-dynamic transient motion, to earthquake slip mediated by elastodynamic rupture. Moreover, our work shows that minor changes in elastic stiffness or frictional rheology can result in dramatic changes in the mode of fault slip. This suggests that a single fault zone could host a slow-slip behavior, when $k' \approx k'_c$, as well as an earthquake, when $k' < k'_c$. This mechanical prediction is consistent with the observation of slow and fast earthquakes occurring on the same fault [Bouchon et al., 2013; Kato et al., 2012; Kato and Nakagawa, 2014; Veedu and Barbot, 2016].

However, slow-slip events often extend to hundreds of kilometers, reaching equivalent earthquake magnitudes of 8 or more. Standard thinking about the relationship between fault rupture area and elastic stiffness [e.g., Okada, 1992] would suggest that slow ruptures, with speeds mediated by K , would accelerate as they expand and the effective elastic stiffness decreases. Thus, there must be another mechanism that limits the rupture patch size and, consequently, elastic stiffness, such that slow events expand as confined slip pulses rather than in accord with the crack model of earthquake rupture [e.g., Scholz, 1982]. Candidate processes include fault zone heterogeneity, which could mediate the effective rupture patch size in a manner that scaled with rupture velocity (and thus K), and rupture fracture energy, which could increase enough near the stability transition to dictate the rupture velocity and thus, ultimately, the rupture patch size and fault slip velocity. We note that tremor migration data [Houston, 2015] show that slow earthquakes generally propagate as slip pulses, where the slipping region is demarked by active tremor. If the active tremor patches are limited in size based on frictional rheology and local elastic stiffness, they would satisfy the predicted relationship between fault slip mode, maximum slip velocity during failure, and the frictional stability parameter K .

6.3. Source Properties of Stick-Slip Events

A detailed analysis of our mechanical data shows a reduction of the risetime with increasing stress drop (Figure 9b). This observation is consistent with the results inferred from natural events, but it also fills the gap between the separate distribution of slow and fast earthquakes [Brodsky and Mori, 2007]. Our stick-slip events occur on an experimental fault of 5 cm in length, and we observe larger coseismic slip for faster earthquake (Figure 12c). This is consistent with the observation that slow events slip less compared to regular earthquakes with similar dimensions.

Since their detection and characterization, slow earthquakes have been classified as a distinct mode of fault slip having a different scaling law $M_0 \approx T$ in comparison with earthquakes $M_0 \approx T^3$, where M_0 is the seismic moment and T is the event duration [Ide et al., 2007]. These different scaling laws imply different driving mechanisms for slow and regular earthquakes. However, the observation that slip modes span a continuum, as we observe, calls into question the existence of two different scaling laws [Peng and Gomborg, 2010; Gomborg et al., 2016]. Our mechanical results (Figures 7–9) coupled with variations of fault zone elastic properties and/or friction constitutive properties during the seismic cycle (Figures 10 and 11) demonstrate a continuous evolution of slip modes from slow to fast earthquakes and suggest that the stiffness ratio K is the key factor driving multimode fault slip behavior.

6.4. V_p Evolution During the Seismic Cycle and Predictability of Time to Failure

Our data show that the state of stress on a fault and the temporal proximity to failure can be monitored by P -wave velocity changes during the seismic cycle. During coseismic slip we observe a significant reduction in V_p of about 2–3% for fast stick-slip events and 1% for slow events coinciding with abrupt acceleration.

We attribute the large reduction in V_p during failure to particle motion and contact rejuvenation. Similar observations of velocity reduction during the coseismic phase have been reported for regular earthquakes in different tectonic environments [Brenguier *et al.*, 2008; Zaccarelli *et al.*, 2011; Soldati *et al.*, 2015; Stehly *et al.*, 2015; Chen *et al.*, 2010] and also for slow events [Rivet *et al.*, 2011, 2014]. For a fault zone of granular and brecciated rock, the magnitude of the elastic wave speed reduction should scale with the degree of brecciation and particle rearrangement (Figure 14a). Thus, near-field measurements such as those in the laboratory, that include only the fault zone, are expected to show larger magnitude ΔV_p than field measurements, which represent a spatial average of the fault zone and surrounding wall rock.

In the laboratory, during the early part of the interseismic period, immediately after the stress drop, wave speed increases and reaches approximately the preslip value within a short time (Figures 10–12). The increase in V_p is consistent with log-time growth, and/or stiffening, of grain contact junctions, consistent with frictional healing [e.g., Scuderi *et al.*, 2014; Carpenter *et al.*, 2016]. We note that similar observations have been made on natural faults [Vidale and Li, 2003; Brenguier *et al.*, 2008; Taira *et al.*, 2015]. However, along natural faults, fault restrengthening promoting an increase in V_p in the postseismic phase can also occur by crack closure and sealing of fractures, possibly facilitated by postseismic fluid flow [e.g., Sibson, 1992] and recovery of micro-crack damage [e.g., Brantut, 2015].

In the laboratory stick-slip events, the onset of inelastic loading coincides with the maximum V_p (Figures 10–12). This occurs before the preparatory stage of failure, as delineated by slip acceleration and the onset of weakening. During this initial stage of weakening and rupture nucleation we observe a reduction in V_p of about 1% and creep acceleration that is more protracted for slow-slip events than for faster events. Our data are consistent with field examples of precursory changes in seismic wave speed, such as those observed only along the San Andreas Fault using borehole seismic data [Niu *et al.*, 2008]. Other seismological studies document similar behaviors; however, the spatiotemporal resolution of the analysis prevents the detection of any precursory V_p signal prior to failure [Brenguier *et al.*, 2008; Stehly *et al.*, 2015].

Comparing our values of V_p variation with those from natural faults we note that our measurements are always larger than those found in nature, which are on the order of 0.1–0.2%. These subtle variations of V_p observed for natural cases might be due to the structural complexity and heterogeneity of these systems compared to the laboratory and/or to the use of remote detectors that include a larger volume of wall rock surrounding the fault compared to the laboratory studies.

6.5. Upscaling to Natural Faults

The systematic V_p evolution recorded during our laboratory seismic cycles shows similarities with V_p changes documented through active seismic surveys and analysis of ambient seismic noise [Brenguier *et al.*, 2008; Chen *et al.*, 2010; Zaccarelli *et al.*, 2011; Soldati *et al.*, 2015; Stehly *et al.*, 2015]. However, it is important to note that while the field observations do not include the full seismic cycle, they often include many of the same features we observe. Therefore, a key question is that of how our experimental results, showing clear precursors to failure, may be upscaled to natural faults.

In the laboratory we characterize the evolution of the fault physical properties in the kHz to MHz range, while in nature the seismic frequency band ranges from MHz to about a few 100 Hz. In addition, the laboratory observations are focused on the fault zone and the region of active shear, whereas the observations in nature include both the fault zone and the surrounding wall rock. Although there are clear differences in the geometry and measurement techniques between nature and laboratory, the resulting V_p evolution is quite similar (Figure 14).

Tectonic faults generally consist of one or more zones of localized strain (the fault core) within a zone of highly fractured rock and secondary faults that together form the damage zone [e.g., Faulkner *et al.*, 2010]. Different techniques have been used to characterize the dimension and architecture of the fault zone structure. Seismic and geodetic data from the Calico fault in the eastern California shear zone reveal a 1.5 km wide zone of reduced seismic velocities and effective elastic moduli [Cochran *et al.*, 2009]. Other seismic studies performed soon after mainshocks have defined a fault zone width of 200–300 m [Vidale and Li, 2003; Ben-Zion *et al.*, 2003]. High-resolution aftershock locations define a fault zone structure of 0.5–1.5 km wide with slip localization along subparallel slipping zones [Valoroso *et al.*, 2014]. Seismicity distributions along strike-slip faults in California define fault zone widths in the range of 100–1500 m

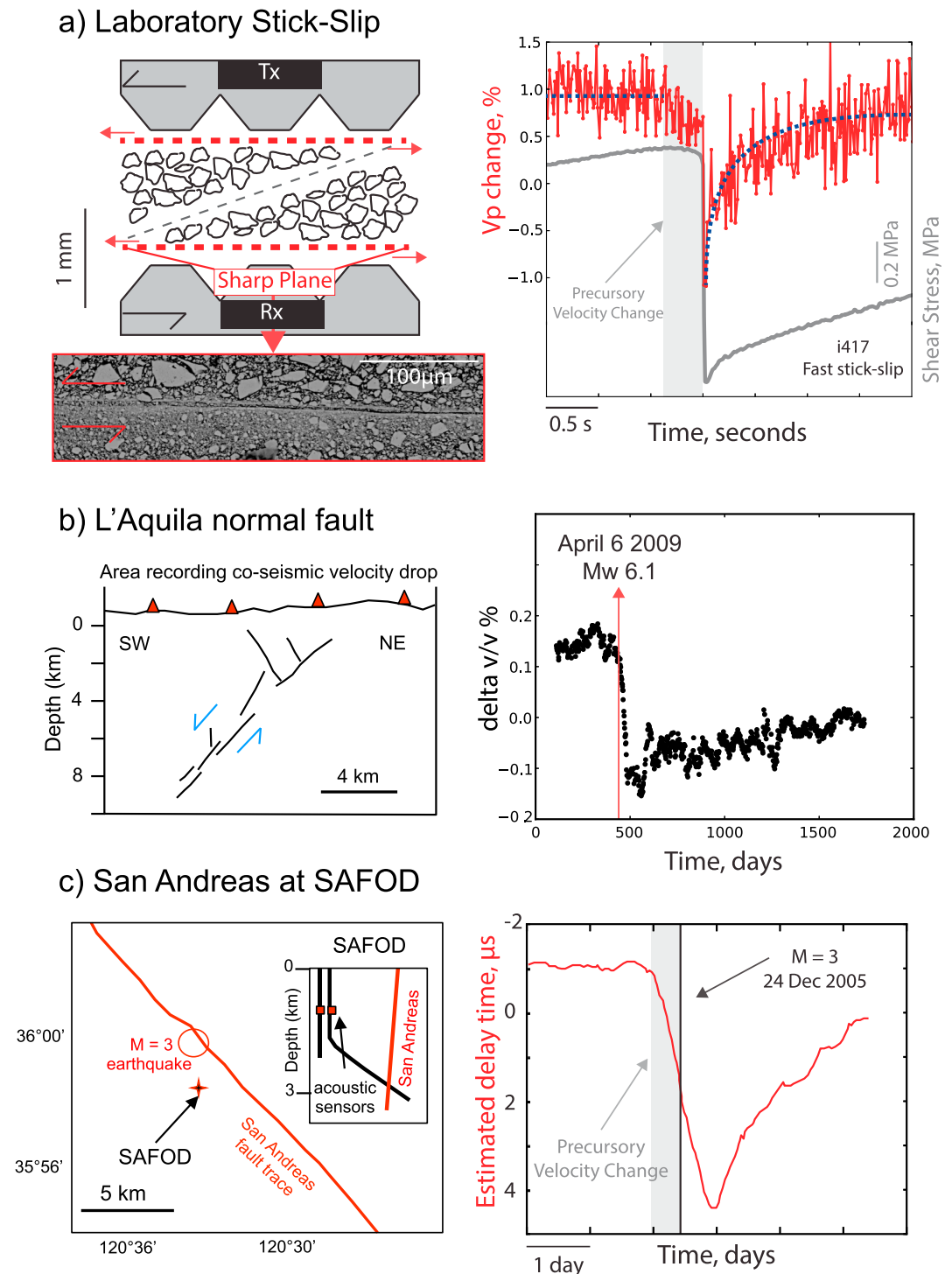


Figure 14. Comparison of seismic velocity changes during the earthquake cycle for a laboratory fault (a) and for two fault slip events in nature: (b) L'Aquila normal fault, studied with ambient noise technique [modified from Soldati *et al.*, 2015], (c) San Andreas Fault, studied through a borehole configuration [modified from Niu *et al.*, 2008].

[Powers and Jordan, 2010]. Geological studies on mature faults in carbonates and granites define a fault zone structure of 1–1.5 km wide with high-strain shear zones that are a meter or more wide [Smith *et al.*, 2015; Collettini *et al.*, 2014b]. Further localization occurs within 1–2 m thick high-strain shear zones possibly during earthquake slip.

Microstructural studies on our experimental faults collected at different strains show that with increasing deformation there is a transition from distributed cataclastic processes at low strain to shear localization and grain size reduction at high strain: grain-size reduction and localization favor the onset of stick slip [Collettini *et al.*, 2016]. The fault structures observed in stick-slip experiments show ~ 2 mm wide shear zones that contain high-strain localization surfaces that are $\leq 2\text{--}4\text{ }\mu\text{m}$ thick (Figure 14a). The geometry of these laboratory faults, with shear localization along $\sim 2\text{ }\mu\text{m}$ shear planes within a $2000\text{ }\mu\text{m}$ wide fault zone structure (i.e., the overall gouge layer thickness), is similar to natural faults where high-strain zones of width ~ 1 m are contained in fault zones that are 1000 m wide. Thus, to a first approximation, the ratio between the localized high-strain zone and surrounding loading medium of the investigated systems is comparable.

During laboratory experiments the adopted frequency, $f = 1$ MHz, for a fault gouge with velocity of about 2 km/s results in a wavelength resolution of $\lambda \leq 2$ mm. Therefore, in the laboratory we have the resolution for the entire thickness of the experimental fault. In this context, we posit that during the linear-elastic loading of a stick-slip event the fault is quasi-stationary (as documented by our mechanical data) and the increase in V_p , that we document, results from variations of the elastic properties of the entire fault (2 mm). In other words, the increase of V_p during the linear loading phase is due to the evolution of the physical properties of both the slipping surface and the fault-loading medium. Then, during the coseismic phase, slip occurs on the highly localized slip surfaces and the reduction in V_p results from the rearrangement of the grain contacts along the slip surface and the loading medium (Figure 14a).

In natural faults, the standard range of studied frequencies is 1–10 Hz, which for a fault zone with $V_p \approx 4$ km/s [Cochran *et al.*, 2009] indicates a wavelength detection range of $400\text{ m} < \lambda < 4000\text{ m}$. With these frequencies it is possible to characterize the evolution of the elastic properties for natural fault zone structure (Figure 14b), such as documented in existing studies of ambient seismic noise [Brenguier *et al.*, 2008; Chen *et al.*, 2010; Soldati *et al.*, 2015; Stehly *et al.*, 2015]. Further details of the fault zone structure could be captured by deploying near fault instruments capable of detecting higher frequencies. For examples, with specially built instruments, capable of firing active pulses at frequency of 2 kHz, Niu *et al.* [2008] showed that the resolution can be up to 1.4 m for an optimum distance between the source and the receiver. In their study, piezoelectric sources and an accelerometer were deployed at 1 km depth inside the pilot and main SAFOD boreholes, respectively. This experiment allowed the detection of *S*-wave velocity variations in the preparatory phase of *M*₁ and *M*₃ earthquakes that occurred a few kilometers away from the instruments (Figure 14c). These variations have been interpreted as the result of the evolution of elastic properties in the fault-loading medium before the earthquakes.

These high-resolution natural observations taken together with our laboratory data, showing that accelerated fault creep causes reduction of seismic velocity during the preparatory phase preceding failure, suggest that real-time monitoring of active faults could aid in the identification of earthquake precursory signals or in early warning systems.

7. Conclusions

Based on friction theory we experimentally reproduced the full spectrum of fault slip behavior and informed the microphysics of frictional stick slip via measurements of *P*-wave velocity. We varied the stiffness ratio *K* and documented a transition from fast stick slip, accompanied by audible energy radiation, to silent slow-slip events. The combination of frictional properties and acoustic data provides a comprehensive view of fault strength evolution during the seismic cycle. We found a systematic relationship between shear stress and *P*-wave velocity for both slow and fast earthquakes, suggesting a common process for the spectrum of fault slip behaviors. Our results indicate that slow slip and fast dynamic rupture can occur on the same fault segment, depending on fault rock frictional properties and local elastic loading conditions. We observe a strong negative correlation between stress drop and event duration, consistent with observations from tectonic faults, where slow earthquakes have systematically lower stress drop and longer duration than regular earthquakes.

We show that acoustic properties and physical processes during earthquake nucleation could provide fundamental insights into the weakening mechanism(s) of tectonic faults. In agreement with seismic surveys on tectonic faults, our data show that the state of stress on a fault can be monitored by *P*-wave velocity changes

during the seismic cycle. The change in V_p velocity shows a similar behavior to the evolution of the mechanical data: (1) V_p initially increases during elastic loading with near-zero fault sliding velocity; (2) V_p reaches a maximum when creep marks the onset of nonlinear elastic deformation; (3) V_p begins to decrease during inelastic deformation for slow events, and only during the preparatory phase for fast events (when stress has already reached the maximum); and (4) V_p shows a clear drop during the weakening phase. Fault creep and the reduction in P -wave velocity indicate that asperity contacts within the fault zone begin to fail prior to macroscopic frictional sliding.

Our data indicate that earthquake nucleation and slip are controlled by the interaction between fault frictional rheology and local elastic properties of the fault zone and surrounding rock. Our observations suggest that the stiffness ratio K incorporates the key parameters for slip stability as applied to tectonic faults and may provide a general mechanism for the spectrum of tectonic fault slip behaviors, possibly acting jointly with dilatancy hardening or other mechanisms (fluid overpressure) to limit rupture speed. The observed reduction in P -wave velocity during the earthquake preparatory phase suggests that if similar mechanisms operate in nature, high-resolution monitoring of the evolution of elastic properties of faults may be a promising avenue for reliable detection of earthquake precursors.

Acknowledgments

We are very grateful to the Editor A. Revil, the Associate Editor A. Schubnel, and two anonymous reviewers for comments and suggestions that significantly improved the manuscript. We thank M. Cocco and J. Leeman for the fruitful discussions and P. Scarlato for the support at the INGV HP-HT laboratory. The data for this paper are available by contacting the corresponding author at elisa.tinti@ingv.it. This research was supported by ERC grant 259256 GLASS to C.C., visiting professor 2015 SAPIENZA grant and grants NSF-EAR1520760 and DE-EE0006762 to C.M., and European Union Horizon 2020 research and innovation program under the Marie Skłodowska-Curie no. 656676 FEAT to M.M.S.

References

- Baumberger, T., F. Heslot, and B. Perrin (1994), Crossover from creep to inertial motion in friction dynamics, *Nature*, *367*, 544–546.
- Baumberger, T., P. Berthoud, and C. Caroli (1999), Physical analysis of the state- and rate-dependent friction law. II. Dynamic friction, *Phys. Rev. B*, *60*, 3928–3939.
- Ben-Zion, Y., Z. Peng, D. Okaya, L. Seeber, J. G. Armbruster, N. Ozer, A. J. Michael, S. Baris, and M. Aktar (2003), A shallow fault-zone structure illuminated by trapped waves in the Karadere-Duzce branch of the North Anatolian Fault, western Turkey, *Geophys. J. Int.*, *152*, 699–717, doi:10.1046/j.1365-246X.2003.01870.x.
- Beroza, G., and S. Ide (2011), Slow earthquakes and nonvolcanic tremor, *Annu. Rev. Earth Planet. Sci.*, *39*, 271–296.
- Bilek, S. L., and T. Lay (1999), Rigidity variations with depth along interplate megathrust faults in subduction zones, *Nature*, *400*, 443–446.
- Bizzarri, A., and M. Cocco (2003), Slip-weakening behavior during the propagation of dynamic ruptures obeying rate- and state-dependent friction laws, *J. Geophys. Res.*, *108*(B8), 2373, doi:10.1029/2002JB002198.
- Blanpied, M. L., C. J. Marone, D. A. Lockner, J. D. Byerlee, and D. P. King (1998), Quantitative measure of the variation in fault rheology due to fluid-rock interactions, *J. Geophys. Res.*, *103*, 9691–9712, doi:10.1029/98JB00162.
- Boatwright, J., and M. Cocco (1996), Frictional constraints on crustal faulting, *J. Geophys. Res.*, *101*, 13,895–13,910, doi:10.1029/96JB00405.
- Bouchon, M., V. Durand, D. Marsan, H. Karabulut, and J. Schmittbuhl (2013), The long precursory phase of most large interplate earthquakes, *Nat. Geosci.*, *6*, 299–302.
- Brace, W., and J. Byerlee (1966), Stick-slip as a mechanism for earthquakes, *Science*, *153*, 990–992.
- Brantut, N. (2015), Time-dependent recovery of microcrack damage and seismic wave speeds in deformed limestone, *J. Geophys. Res. Solid Earth*, *120*, 8088–8109, doi:10.1002/2015JB012324.
- Brenguier, F., M. Campillo, C. Hadziioannou, N. M. Shapiro, R. M. Nadeau, and E. Larose (2008), Postseismic relaxation along the San Andreas Fault at Parkfield from continuous seismological observations, *Science*, *321*(5895), 1478–1481, doi:10.1126/science.1160943.
- Brodsky, E. E., and J. Mori (2007), Creep events slip less than ordinary earthquakes, *Geophys. Res. Lett.*, *34*, L16309, doi:10.1029/2007GL030917.
- Brodsky, E., and T. Lay (2014), Recognizing foreshocks from the 1 April 2014 Chile earthquake, *Science*, *344*, 700–702, doi:10.1126/science.1255202.
- Carpenter, B. M., M. J. Ikari, and C. Marone (2016), Laboratory observations of time-dependent frictional strengthening and stress relaxation in natural and synthetic fault gouges, *J. Geophys. Res. Solid Earth*, *121*, 1183–1201, doi:10.1002/2015JB012136.
- Chen, J. H., B. Froment, Q. Y. Liu, and M. Campillo (2010), Distribution of seismic wave speed changes associated with the 12 May 2008 Mw 7.9 Wenchuan earthquake, *Geophys. Res. Lett.*, *37*, L18302, doi:10.1029/2010GL044582.
- Cochran, E. S., Y. G. Li, P. M. Shearer, S. Barbot, Y. Fialko, and J. E. Vidale (2009), Seismic and geodetic evidence for extensive, long-lived fault damage zones, *Geology*, *37*, 315–318.
- Collettini, C., G. Di Stefano, B. Carpenter, P. Scarlato, T. Tesei, S. Mollo, F. Trippetta, C. Marone, G. Romeo, and L. Chiaraluce (2014a), A novel and versatile apparatus for brittle rock deformation, *Int. J. Rock Mech. Min. Sci.*, *66*, 114–123, doi:10.1016/j.ijrmm.2013.12.005.
- Collettini, C., B. M. Carpenter, C. Viti, F. Cruciani, S. Molto, T. Tesei, F. Trippetta, L. Valoroso, and L. Chiaraluce (2014b), Fault structure and slip localization in carbonate bearing normal faults: An example from the Northern Apennines of Italy, *J. Struct. Geol.*, *67*, 154–166, doi:10.1016/j.jsg.2014.07.017.
- Collettini, C., M. Scuderi, C. Viti, E. Tinti, and C. Marone (2016), Microstructural evolution from stable sliding to fast stick slip: Insights from rock deformation experiments on quartz European Geoscience Union, Vienna, April 2016.
- Crescentini, L., A. Amoroso, and R. Scarpa (1999), Constraints on slow earthquake dynamics from a swarm in Central Italy, *Science*, *286*, 2132–2134.
- Das, I., and M. D. Zoback (2013), Long-period, long-duration seismic events during hydraulic fracture stimulation of a shale gas reservoir, *Geophysics*, *30*(7), 778–786, doi:10.1190/1.3609093.
- Di Toro, G., R. Han, T. Hirose, N. De Paola, S. Nielsen, K. Mizoguchi, F. Ferri, M. Cocco, and T. Shimamoto (2011), Fault lubrication during earthquakes, *Nature*, *471*(7339), 494–498.
- Dieterich, J. H. (1979), Modeling of rock friction: 1. Experimental results and constitutive equations, *J. Geophys. Res.*, *84*(B5), 2161–2168, doi:10.1029/JB084iB05p02161.
- Dieterich, J. H. (1981), Constitutive properties of faults with simulated gouge, in *Mechanical Behavior of Crustal Rocks*, *Geophys. Monogr. Ser.*, vol. 24, edited by N. L. Carter et al., pp. 102–120, AGU, Washington, D. C.
- Dieterich, J. H., and B. D. Kilgore (1994), Direct observation of frictional contacts: New insights for state-dependent properties, *Pure Appl. Geophys.*, *143*, 283–302, doi:10.1007/BF00874332.

- Ekstrom, G., M. Nettles, and G. A. Abers (2003), Glacial earthquakes, *Science*, 302(5645), 622–624, doi:10.1126/science.1088057.
- Faulkner, D. R., C. A. L. Jackson, R. J. Lunn, R. W. Schlische, Z. K. Shipton, C. A. J. Wibberley, and M. O. Withjack (2010), A review of recent developments concerning the structure, mechanics and fluid flow properties of fault zones, *J. Struct. Geol.*, 32(11), 1557–1575, doi:10.1016/j.jsg.2010.06.009.
- Fukuyama, E., T. Mikumo, and K. B. Olsen (2003), Estimation of the critical slip-weakening distance: Theoretical background, *Bull. Seismol. Soc. Am.*, 93, 1835–1840.
- Gomberg, J., A. Wech, K. Creager, K. Obara, and D. Agnew (2016), Reconsidering earthquake scaling, *Geophys. Res. Lett.*, 43, 6243–6251, doi:10.1002/2016GL069967.
- Gu, J. C., J. R. Rice, A. L. Ruina, and S. T. Tse (1984), Slip motion and stability of a single degree of freedom elastic system with rate and state dependent friction, *J. Mech. Phys. Solids*, 32(3), 167–196.
- Guglielmi, Y., F. Cappa, J. Avouac, P. Henry, and D. Elsworth (2015), Seismicity triggered by fluid injection-induced aseismic slip, *Science*, 348, 1224–1226.
- Hirose, H., and K. Obara (2005), Repeating short- and long-term low slip events with deep tremor activity, around the Bungo channel region, southwest Japan, *Earth Planets Space*, 57, 961–972.
- Houston, H. (2015), Low friction and fault weakening revealed by rising sensitivity of tremor to tidal stress, *Nat. Geosci.*, 8, 409–415.
- Ide, S., G. C. Beroza, D. R. Shelly, and T. Uchide (2007), A scaling law for slow earthquakes, *Nature*, 447(7140), 76–79, doi:10.1038/nature05780.
- Ikari, M. J., C. Marone, D. M. Saffer, and A. J. Kopf (2013), Slip weakening as a mechanism for slow earthquakes, *Nat. Geosci.*, 6, 468–472, doi:10.1038/ngeo1818.
- Ikari, M. J., Y. Ito, K. Ujiie, and A. J. Kopf (2015), Spectrum of slip behaviour in Tohoku fault zone samples at plate tectonic slip rates, *Nat. Geosci.*, 1–6, doi:10.1038/ngeo2547.
- Ito, Y., et al. (2013), Episodic slow slip events in the Japan subduction zone before the 2011 Tohoku-Oki earthquake, *Tectonophysics*, 600, 14–26.
- Jia, X., C. Caroli, and B. Velicky (1999), Ultrasound propagation in externally stressed granular media, *Phys. Rev. Lett.*, 82(9), 1863–1866, doi:10.1103/PhysRevLett.82.1863.
- Johnson, P. A., B. Ferdowsi, B. M. Kaproth, M. Scuderi, M. Griffo, J. Carmeliet, R. A. Guyer, P.-Y. Le Bas, D. T. Trugman, and C. Marone (2013), Acoustic emission and microslip precursors to stick-slip failure in sheared granular material, *Geophys. Res. Lett.*, 40, 5627–5631, doi:10.1002/2013GL057848.
- Kame, N., K. Nagata, M. Nakatani, and T. Kusakabe (2014), Feasibility of acoustic monitoring of strength drop precursory to earthquake occurrence, *Earth Planets Space*, 66(1), 1–12.
- Kaproth, B. M., and C. Marone (2013), Slow earthquakes, preseismic velocity changes, and the origin of slow frictional stick-slip, *Science*, 341(6151), 1229–1232, doi:10.1126/science.1239577.
- Kato, A., and S. Nakagawa (2014), Multiple slow-slip events during a foreshock sequence of the 2014 Iquique, Chile Mw 8.1 earthquake, *Geophys. Res. Lett.*, 41, 5420–5427, doi:10.1007/s13398-014-0173-7.2.
- Kato, A., et al. (2012), Propagation of slow slip leading up to the 2011 Mw 9.0 Tohoku-Oki earthquake, *Science*, 335(6069), 705–708, doi:10.1126/science.1215141.
- Knuth, M. W., H. J. Tobin, and C. Marone (2013), Evolution of ultrasonic velocity and dynamic elastic moduli with shear strain in granular layers, *Granular Matter*, 15(5), 499–515, doi:10.1007/s10035-013-0420-1.
- Leeman, J. R., Saffer, D. M., Scuderi, M. M., and C. Marone (2016), Laboratory observations of slow earthquakes and the spectrum of tectonic fault slip modes, *Nat. Commun.*, 7, 11104, doi:10.1038/ncomms11104.
- Liu, Y., and J. R. Rice (2007), Spontaneous and triggered aseismic deformation transients in a subduction fault model, *J. Geophys. Res.*, 112, B09404, doi:10.1029/2007JB004930.
- Lykourafitis, G., A. Rosakis, and G. Ravichandran (2006), Self-healing pulse-like shear ruptures in the laboratory, *Science*, 313, 1765–1768.
- Mai, P. M., and K. K. S. Thingbaijam (2014), SRCMOD: An online database of finite-fault rupture models, *Seismol. Res. Lett.*, 85(6), 1348–1357, doi:10.1785/0220140077.
- Marone, C. (1998), Laboratory-derived friction laws and their application to seismic faulting, *Annu. Rev. Earth Planet. Sci.*, 26(1), 643–696.
- Marone, C., and B. Kilgore (1993), Scaling of the critical slip distance for seismic faulting with shear strain in fault zones, *Nature*, 362, 618–621.
- Marone, C., M. Cocco, E. Richardson, and E. Tinti (2009), The critical slip distance for seismic and aseismic fault zones of finite width, in *Fault-Zone Structure and Earthquake Rupture Dynamics*, Int. Geophys. Ser., vol. 94, edited by E. Fukuyama, pp. 135–162, Elsevier, Amsterdam.
- McLaskey, G. C., B. D. Kilgore, and N. M. Beeler (2015), Slip-pulse rupture behavior on a 2 m granite fault, *Geophys. Res. Lett.*, 42, 7039–7045, doi:10.1002/2015GL065207.
- Nagata, K., M. Nakatani, and S. Yoshida (2008), Monitoring frictional strength with acoustic wave transmission, *Geophys. Res. Lett.*, 35, L06310, doi:10.1029/2007GL033146.
- Nagata, K., M. Nakatani, and S. Yoshida (2012), A revised rate-and state-dependent friction law obtained by constraining constitutive and evolution laws separately with laboratory data, *J. Geophys. Res.*, 117, B02314, doi:10.1029/2011JB008818.
- Niu, F., P. G. Silver, T. M. Daley, X. Cheng, and E. L. Majer (2008), Preseismic velocity changes observed from active source monitoring at the Parkfield SAFOD drill site, *Nature*, 454, 204–208, doi:10.1038/nature07111.
- Obara, K. (2002), Nonvolcanic deep tremor associated with subduction in southwest Japan, *Science*, 296, 1679–1681.
- Obara, K., and A. Kato (2016), Connecting slow earthquakes to huge earthquakes, *Science*, 353(6296), 253–257, doi:10.1126/science.aaf1512.
- Okada, Y. (1992), Internal deformations due to shear and tensile faults in a half-space, *Bull. Seismol. Soc. Am.*, 82(2), 1018–1040.
- Palmer, A. C., and J. R. Rice (1973), The growth of slip surfaces in the progressive failure of over-consolidated clay, *Proc. R. Soc. London, Ser. A*, 332, 527–548.
- Passelègue, F. X., A. Schubnel, S. Nielsen, H. S. Bhat, D. Deldicque, and R. Madariaga (2016a), Dynamic rupture processes inferred from laboratory microearthquakes, *J. Geophys. Res. Solid Earth*, 121, 4343–4365, doi:10.1002/2015JB012694.
- Passelègue, F. X., E. Spagnuolo, S. Nielsen, and G. Di Toro (2016b), Frictional evolution, acoustic emissions activity and off-fault damage in simulated faults sheared at seismic slip rates, *J. Geophys. Res. Solid Earth*, 121, 7490–7513, doi:10.1002/2016JB012988.
- Peng, Z., and J. Gomberg (2010), An integrated perspective of the continuum between earthquakes and slow-slip phenomena, *Nat. Geosci.*, 3(9), 599–607, doi:10.1038/ngeo940.
- Powers, P. M., and T. H. Jordan (2010), Distribution of seismicity across strike-slip faults in California, *J. Geophys. Res.*, 115, B05305, doi:10.1029/2008JB006234.
- Reinen, L., and J. Weeks (1993), Determination of rock friction constitutive parameters using an iterative least squares inversion method, *J. Geophys. Res.*, 98(B9), 15,937–15,950, doi:10.1029/93JB00780.

- Rice, J. R., and A. Ruina (1983), Stability of steady frictional slipping, *J. Appl. Mech.*, *50*, 343–3459.
- Rivet, D., M. Campillo, N. M. Shapiro, V. Cruz-Atienza, M. Radiguet, N. Cotte, and V. Kostoglodov (2011), Seismic evidence of nonlinear crustal deformation during a large slow slip event in Mexico, *Geophys. Res. Lett.*, *38*, L08308, doi:10.1029/2011GL047151.
- Rivet, D., et al. (2014), Seismic velocity changes, strain rate and non-volcanic tremors during the 2009–2010 slow slip event in Guerrero, Mexico, *Geophys. J. Int.*, *196*, 447–460.
- Rogers, G., and H. Dragert (2003), Episodic tremor and slip on the Cascadia subduction zone: The chatter of silent slip, *Science*, *300*, 1942–1943.
- Rosakis, A. J., O. Samudrala, and D. Coker (1999), Cracks faster than the shear wave speed, *Science*, *284*, 1337–1340.
- Rubin, A. M. (2008), Episodic slow slip events and rate-and-state friction, *J. Geophys. Res.*, *113*, B11414, doi:10.1029/2008JB005642.
- Rubinstein, J. L., D. R. Shelly, and W. L. Ellsworth (2010), Non-volcanic tremor: A window into the roots of fault zones, in *New Frontiers in Integrated Solid Earth Sciences*, pp. 287–314, Springer, Netherlands.
- Ruina, A. (1983), Slip instability and state variable friction laws, *J. Geophys. Res.*, *88*(B12), 10,359–10,370, doi:10.1029/JB088B12p10359.
- Ruiz, S., M. Metois, A. Fuenzalida, J. Ruiz, F. Leyton, R. Grandin, C. Vigny, R. Madariaga, and J. Campos (2014), Intense foreshocks and a slow slip event preceded the 2014 Iquique Mw 8.1 earthquake, *Science*, *345*(6201), 1165–1169, doi:10.1126/science.1256074.
- Sacks, I. S., S. Suyehiro, A. T. Linde, and J. A. Snoke (1978), Slow earthquakes and stress redistribution, *Nature*, *275*, 599–602.
- Saffer, D. M., and C. Marone (2003), Comparison of smectite- and illite-rich gouge frictional properties: Application to the updip limit of the seismogenic zone along subduction megathrusts, *Earth Planet. Sci. Lett.*, *215*, 219–235.
- Scholz, C. H. (1982), Scaling laws for large earthquakes: Consequences for physical models, *Bull. Seismol. Soc. Am.*, *72*(1), 1–14.
- Scholz, C. H. (1998), Earthquakes and friction laws, *Nature*, *391*, 37–42, doi:10.1038/34097.
- Scholz, C. H. (2002), *The Mechanics of Earthquakes and Faulting*, Cambridge Univ. Press, New York.
- Scholz, C., P. Molnar, and T. Johnson (1972), Detailed studies of frictional sliding of granite and implications for the earthquake mechanism, *J. Geophys. Res.*, *77*, 6392–6406, doi:10.1029/JB077i032p06392.
- Schubnel, A., P. M. Benson, B. D. Thompson, J. F. Hazzard, and R. P. Young (2006), Quantifying damage, saturation and anisotropy in cracked rocks by inverting elastic wave velocities, *Pure Appl. Geophys.*, *163*, 947–973.
- Schulz, W. H., J. W. Kean, and G. Wang (2009), Landslide movement in southwest Colorado triggered by atmospheric tides, *Nat. Geosci.*, *2*, 863–866, doi:10.1038/ngeo659.
- Schwartz, S., and J. Rokosky (2007), Slow slip events and seismic tremor at circum-Pacific subduction zones, *Rev. Geophys.*, *45*, RG3004, doi:10.1029/2006RG000208.
- Scuderi, M. M., and C. Collettini (2016), The role of fluid pressure in induced vs. triggered seismicity: Insights from rock deformation experiments on carbonates, *Sci. Rep.*, *6*, 24852, doi:10.1038/srep24852.
- Scuderi, M. M., B. M. Carpenter, and C. Marone (2014), Physicochemical processes of frictional healing: Effects of water on stick-slip stress drop and friction of granular fault gouge, *J. Geophys. Res. Solid Earth*, *119*, 4090–4105, doi:10.1002/2013JB010641.
- Scuderi, M. M., C. Marone, E. Tinti, G. Di Stefano, and C. Collettini (2016), Precursory changes in seismic velocity for the spectrum of earthquake failure modes, *Nat. Geosci.*, *9*, 695–700, doi:10.1038/ngeo2775.
- Segall, P., and J. Rice (1995), Dilatancy, compaction and slip instability of a fluid-infiltrated fault, *J. Geophys. Res.*, *100*(B11), 22,155–22,171, doi:10.1029/95JB02403.
- Segall, P., A. M. Rubin, A. M. Bradley, and J. R. Rice (2010), Dilatant strengthening as a mechanism for slow slip events, *J. Geophys. Res.*, *115*, B12305, doi:10.1029/2010JB007449.
- Shelly, D. R. (2009), Possible deep fault slip preceding the 2004 Parkfield earthquake, inferred from detailed observations of tectonic tremor, *Geophys. Res. Lett.*, *36*, L17318, doi:10.1029/2009GL039589.
- Shelly, D. R., G. C. Beroza, S. Ide, and S. Nakamura (2006), Low-frequency earthquakes in Shikoku, Japan, and their relationship to episodic tremor and slip, *Nature*, *442*, 188–191.
- Sibson, R. H. (1992), Implications of fault-valve behavior for rupture nucleation and recurrence, *Tectonophysics*, *18*, 1031–1042.
- Smith, S. A. F., S. Nielsen, and G. Di Toro (2015), Strain localization and the onset of dynamic weakening in calcite fault gouge, *Earth Planet. Sci. Lett.*, *413*, 25–36, doi:10.1016/j.epsl.2014.12.043.
- Soldati, G., L. Zaccarelli, L. Faenza, and A. Michelini (2015), Monitoring of crustal seismic velocity variations in the L'Aquila fault zone inferred from noise cross-correlation, *Geophys. J. Int.*, *202*, 604–611, doi:10.1093/gji/ggv172.
- Stehly, L., B. Froment, M. Campillo, Q. Y. Liu, and J. H. Chen (2015), Monitoring seismic wave velocity changes associated with the Mw 7.9 Wenchuan earthquake: Increasing the temporal resolution using curvelet filters, *Geophys. J. Int.*, *207*(3), 1939–1949, doi:10.1093/gji/ggv110.
- Taira, T., F. Brenguier, and Q. Kong (2015), Ambient noise-based monitoring of seismic velocity changes associated with the 2014 Mw 6.0 South Napa earthquake, *Geophys. Res. Lett.*, *42*, 6997–7004, doi:10.1002/2015GL065308.
- Tanikawa, W., M. Sakaguchi, O. Tada, and T. Hirose (2010), Influence of fault slip rate on shear-induced permeability, *J. Geophys. Res.*, *115*, B07412, doi:10.1029/2009JB007013.
- Tinti, E., A. Bizzarri, A. Piatanesi, and M. Cocco (2004), Estimates of slip weakening distance for different dynamic rupture models, *Geophys. Res. Lett.*, *31*, L02611, doi:10.1029/2003GL018811.
- Tinti, E., M. Cocco, E. Fukuyama, and A. Piatanesi (2009), Dependence of slip weakening distance (D_c) on final slip during dynamic rupture of earthquakes, *Geophys. J. Int.*, *177*(3), 1205–1220.
- Tse, S. T., and J. R. Rice (1986), Crustal earthquake instability in relation to the depth variation of frictional slip properties, *J. Geophys. Res.*, *91*(B9), 9452–9472, doi:10.1029/JB091iB09p09452.
- Valeroso, L., L. Chiaraluce, and C. Collettini (2014), Earthquakes and fault zone structure, *Geology*, *42*, 343–346.
- Veedu, D. M., and S. Barbot (2016), The Parkfield tremors reveal slow and fast ruptures on the same asperity, *Nature*, *532*, 361–365.
- Vidale, J. E., and Y.-G. Li (2003), Damage to the shallow Landers fault from the nearby Hector Mine earthquake, *Nature*, *421*, 524–526, doi:10.1038/nature01354.
- Wallace, L. M., S. C. Webb, Y. Ito, K. Mochizuki, R. Hino, S. Henrys, S. Y. Schwartz, and A. F. Sheehan (2016), Slowslip near the trench at the Hikurangi subduction zone, New Zealand, *Science*, *352*(6286), 701–704, doi:10.1126/science.aaf2349.
- Xia, K., A. Rosakis, and H. Kanamori (2004), Laboratory earthquakes: The sub-Rayleigh-to-supershear rupture transition, *Science*, *303*, 1859–1861.
- Zaccarelli, L., N. M. Shapiro, L. Faenza, G. Soldati, and A. Michelini (2011), Variations of crustal elastic properties during the 2009 L'Aquila earthquake inferred from cross-correlations of ambient seismic noise, *Geophys. Res. Lett.*, *38*, L24304, doi:10.1029/2011GL049750.
- Zoback, M. D., A. Kohli, I. Das, and M. McClure (2012), The importance of slow slip on faults during hydraulic fracturing stimulation of shale gas reservoirs, *SPE* 155476, doi:10.2118/155476-MS.